N73 32772

IIT Research Institute
10 West 35 Street, Chicago, Illinois 60616
312/225-9630

April 4, 1973

Dr. William E. Brunk
Code SL
NASA Headquarters
Washington, D.C. 20546

Subject: Final Report Contract NASW-2363
"Ground Based Planetary Research"

Dear Dr. Brunk:

This report contains the results of the observations and analysis carried out under contract NASW-2363 during the period from April 26, 1972 to April 4, 1973. Not all of the goals initially proposed have been reached due in part to observational problems and in part due to the problems of analysis. These difficulties have been detailed in previous quarterly reports.

Two significant papers have resulted, however, and pre-publication drafts are included as appendices to this report. Appendix A, "IR Spectrophotometry of Jupiter and Saturn", Bender and McCarthy, and Appendix B, "Scattering Mean Free Path in the Uranian Atmosphere", Price, are being submitted to Icarus for publication.

Respectfully submitted,
IIT RESEARCH INSTITUTE

C. A. Stone, Director
Physics Research Division

CAS:jg

Page Intentionally Left Blank

APPENDIX A

IR SPECTROPHOTOMETRY OF JUPITER AND SATURN

Alan B. Binder
Donald W. McCarthy, Jr.

Page Intentionally Left Blank

ABSTRACT

High spatial resolution spectrophotometric observations made in the wavelength region $\lambda\lambda$ 0.6 - 2.0 μm are used to study the Jovian and Saturnian limb darkening at 0^{o} phase angle. Limb darkening coefficients (k) of the Minnaert function are derived for the cloud layers of both planets. A value of k = 1.0 is found for Jupiter over the entire disk while values of between 0.75 and 0.90 are found for different latitudes for Saturn. These data are used to derive geometric albedoes (G) for the various belts, zones, spots and regions observed on Jupiter and Saturn. These values of G and k are in turn used to show that an isotropic scattering model is invalid for Jupiter and that at least an asymmetric scattering function, such as the Euler function $[\tilde{\omega}_0 (1 + a \cos\theta)]$, is needed to fit the Jovian data. The Jovian scattering function is found to generally vary between $0.960 (1 + 0.85 \cos\theta)$ and $0.994 (1 + 0.42 \cos\theta)$ as a function of wavelength and the feature observed. The Saturn geometric albedoes and values of k indicate that Euler's function fails to adequately model the scattering properties of the Saturnian clouds. As a result it is suggested that simple scattering theory may not apply to the Saturn clouds or that they are better represented by a cumulus cloud model.

Page Intentionally Left Blank

IR SPECTROPHOTOMETRY OF JUPITER & SATURN

This paper reports the results obtained from a series of spectrophotometric observations of Jupiter and Saturn in the wavelength region λλ 0.6 to 2.0 μm. The program was carried out in order to obtain information on the spectral albedoes and limb darkening properties of these Jovian planets. The empirical data provides a basis for determining the wavelength dependent single scattering albedo ($\tilde{\omega}_0$) and scattering function for the cloud layers of each belt, zone or spot observed on Jupiter. Models for the clouds of Saturn are also suggested.

I. INSTRUMENTATION AND OBSERVATIONS

The observations were carried out with the Kitt Peak Observatory 50 inch (127 cm) reflector and a 10 channel PbS spectrophotometer which acquires data at 10 wavelengths simultaneously (Binder and Jones, 1969). The wavelengths observed and the passbands are given in Table 1. The observations of Jupiter were made with a $2''.76$ entrance aperture so that the geometric resolution was on average 1/16 that of the equatorial diameter (39" to 47") of the planet. Due to seeing effects and guiding errors during the 1 minute integration periods used, the effective resolution was reduced to 3" to 4", which was still sufficient to isolate the major bands, zones, and the Great Red Spot.

Jupiter was observed on May 11, 1971, April 7, 1972 and on June 25, 1972. The phase angles of Jupiter and these dates were $2^{\circ}.4$ $10^{\circ}.8$ and $0^{\circ}.1$ respectively. Observations of λ Serpentis, a G0V object, were made to provide calibration data.

Saturn was observed with a $1''.84$ entrance diaphragm and hence the geometric resolution was about 1/11 the equatorial diameter (21") of the planet. As in the case of Jupiter, this resolution was degraded to 2" to 3" by seeing effects and guiding errors during the 2 minute integration periods used to make the observations.

Saturn was observed on the 25, 27, and 28 of November, 1972 when the phase angle varied between $0^{\circ}.2$ and $0^{\circ}.4$. The stars, ϵ Gemorium (G 8 1b) and η Pegasus (G 2II - III + F?) provided calibration data for the Saturn observations.

TABLE 1. PASSBAND CENTERS AND PASSBAND WIDTHS OF THE 10 CHANNEL PbS SPECTROPHOTOMETER

Detector No.	Passband Center, μm	Passband Width, μm
1	0.594	0.029
2	0.640	0.021
3	0.725	0.034
4	0.823	0.059
5	0.964	0.084
6	1.077	0.093
7	1.240	0.094
8	1.442	0.084
9	1.554	0.071
10	1.992	0.074

II. NUMERICAL REDUCTION

The numerical reduction of the data was carried out using the Kitt Peak National Observatory computer facilities. The data reduction procedures used for reducing the Jupiter and Saturn data are similar to those used for Mars as described by Binder and Jones (1972). The programs (i.e. Jupiter/Saturn vs Mars) differ only in that the geometric computations take into account the oblateness of Jupiter and Saturn, while Mars is treated as a sphere.

Briefly, the program was used to convert the observed x and y coordinates of each spot for terrestrial atmospheric dispersion and then to compute a series of zenographic (and Saturnographic) parameters [latitude, longitude, cosine of the angle of incidence (i), cosine of the angle of emission (e), and reference air mass (AM)]for each point and to correct the photometric data for extinction, etc. In addition, the stellar data were corrected for wavelength dependent and seeing light losses since they were observed with 4".4 entrance diaphragm (the largest that can be used with the 10 channel system); the procedures followed are discussed by Young (1970). Also, while the stars observed are solar or near solar types, corrections to their observed colors were necessary to account for the differences between them and the sun. The data of Johnson (1965) and Johnson et al. (1966) were used to make these corrections.

III. APPLICABILITY OF THE MINNAERT FUNCTION FOR LIMB DARKENING STUDIES

In an earlier paper (Binder, 1972: hereafter referred to as paper 1) showed that the Minnaert function could be used to describe the Jovian limb darkening in the 1.5 μm region and that, when the effects of the strong 1.5 μm CH_4 and NH_3 absorptions were accounted for, the cloud layer appeared to behave like a Lambertian reflector. As a result of this work, we were interested in testing the general applicability of the Minnaert function to both Jupiter and Saturn over a wide range of wavelengths, to obtain a more precise determination of the limb darkening of the cloud layers, and to determine if the Minnaert function could also be used to compare theoretical scattering models with the observational data.

The function has the form

$$B_s = B_o \cos^k i \cos^{k-1} e \qquad (1)$$

where B_s is the brightness of the surface element, B_o the brightness of a surface element at $\cos^k i \cos^{k-1} e = 1$, i the angle of incidence, e the angle of emission, and k a dimensionless coefficient. Both B_o and k are functions of the wavelength (λ) and the phase angle (α). This equation can be written in the linear form,

$$\log (B_s \cdot \cos e) = \log B_o + k \log (\cos i \cdot \cos e) \qquad (2)$$

so that k, which we shall refer to as the limb darkening coefficient, can be readily found from log-log plots of the data as demonstrated in paper 1 (see Figures 8 and 9) and in Figures 1 and 2 of this paper using the new Jupiter and Saturn data.

In addition to testing the general applicability of the Minneart function to fit empirical limb darkening data (see details in section IV below) we find that the function also satisfactorily represents the theoretical limb darkening for a variety of different Euler scattering models as computed by Horak and Little (1965), see Figure 3. As a result of these exercises, we find that the Minnaert function is an effective tool for representing and comparing empirical and theoretical limb darkening data.

In addition, the Minnaert function is useful for deriving Harris' limb darkening parameter x (1961), and the geometric albedo (G) of small areas on the disks of Jupiter and Saturn [both x and G are needed to determine single scattering albedoe ($\tilde{\omega}_0$) and scattering function of the clouds]. In the first case, Harris defines x as

$$x = \frac{2 B_c}{B_o} \qquad (3)$$

where B_c is the brightness of a surface element (B_s) at the characteristic point, i.e. at $\cos i = 0.5$, and B_o is the brightness of the center of the disk. When $\alpha = 0$,

i.e. when cos i = cos e,

$$B_s = B_o \cos^{2k-1} i \quad . \tag{4}$$

Thus, from (3) and (4)

$$x = 2\,(0.5)^{2k-1} \quad . \tag{5}$$

The geometric albedo (G) of a belt, zone or spot is derived from its brightness at the center of the disk, as computed from equation (1), as follows:

$$G = \frac{\int^{s} B_s ds}{\int^{s} F ds} \tag{6}$$

where F is the incident solar flux per unit area.

By equation (4) and (6), and assuming a circular disk,

$$G = \frac{2\pi \int_o^1 r\, B_o \cos^{2k-1} i\, dr}{2\pi\, F \int_o^1 r\, dr} \tag{7}$$

where F is the flux per unit area. Now

$$\cos i = \sqrt{1-r^2} \quad , \tag{8}$$

by (7) and (8)

$$G = \frac{B_o \int_o^1 r\,(1-r^2)^{k-1/2}\, dr}{F \int_o^1 r\, dr} \tag{9}$$

Thus $$G = \frac{2}{2k+1} \left(\frac{B_o}{F}\right) \tag{10}$$

However B_o/F is the normal albedo (N) of the point [as derived from the high spatial resolution spectrophotometric data (Binder and Jones, 1972)] so the geometric albedo of any small point is

$$G = \frac{2N}{2k+1} \tag{11}$$

For no limb darkening, i.e. k = 0.5, G = N, and for Lambertian limb darkening, i.e. k = 1.0, G = 2N/3.

Thus, via the Minnaert function and equations (5) and (11), spectrophotometric measurements of small areas of a planet can be readily converted into the quantities needed to study the scattering properties of the belts, zones and spots of the planets, even though the quantities themselves are not observed directly.

IV. JOVIAN AND SATURNIAN LIMB DARKENING

As indicated in Section III, and illustrated inpart in Figures 1 and 2, the limb darkening of all zones, belts, regions and spots of Jupiter and Saturn can be satisfactorily represented by the Minnaert function at all wavelengths.* Because of the axial symmetry of the markings of Jupiter and Saturn and because of the differences in center to limb and center to pole variations of the CH_4 and (for Jupiter) NH_3 absorptions (Hess, 1953; Münch and Younkin, 1964; Teifel 1969; Owen and Mason 1969; Moroz and Cruikshank 1969; and Binder 1972) the E-W traces (i.e. traces taken along belts, zones and spots) must be treated separately from N-S traces taken along the central meridian. Table 2 and Figures 4a and 4b give the values of k for the various features observed and the averages of the N-S and E-W data respectively.

As was found in the earlier study of the limb darkening of the 1.5 μm region (paper 1) and as apparent in Table 2, the limb darkening of the belts, zones, etc. are identical at $\alpha \tilde{=} 0$ to within the uncertainty of the measurements, i.e. Jupiter has uniform E-W limb darkening over the entire disk.

---

* Generally, however, the signal to noise for the 1.44 μm and 1.99 μm passbands is too poor for good values of k to be determined. This is the case since both of these passbands lie in very deep NH_3 and CH_4 absorption bands and telluric H_2O bands.

TABLE 2: LIMB DARKENING COEFFICIENTS FOR JUPITER AND SATURN

Wavelength (μm)			0.59	0.64	0.72	0.82	0.96	1.08	1.24	1.44	1.55	1.99
Obj.	Date	α Trace Lat.										
Jup.	5/11/71	2°.4 N-S	1.03	1.00	1.04	1.08	1.18	1.05	1.22	~1.9	1.23	~2.0
Jup.	4/7/72	10°.8 N-S	1.05	1.04	1.03	1.12	1.23	1.14	1.30	~2.0	1.17	~2.2
		E-W +3°(ER)	.99	.99	.95	.96	.88	.85	.78	~ .8	.77	~ .7
Jup.	6/25/72	0°.1 N-S	.95	1.00	1.05	1.06	1.10	1.16	1.38	~1.7	1.40	~1.7
		E-W+2°(ER)	.98	1.01	1.03	1.02	.96	.97	.90	~ .9	.86	~ .8
		E-W-15°(STrZ)	1.01	1.00	1.01	.95	1.00	.98	.90	----	.76	----
		E-W+52°(NPR)	.99	.98	1.03	1.00	1.04	.91	.89	----	.67	----
		E-W-20°(GRS)	1.00	.99	.93	1.00	.99	.94	.90	~1.0	.82	~1.0
Jup.	Mean k	N-S	1.01±5	1.01±3	1.04±2	1.09±4	1.17±7	1.12±7	1.30±8	~1.9	1.27±13	~2.0
	For $\alpha \simeq 0$	E-W	1.00±2	1.00±2	1.00±5	.99±4	1.00±4	.95±3	.90±2	~ .9	.78±10	~ .9
Sat.	11/25/72	0°.2 N-S	.90	.93	.99	.98	.98	1.03	1.25	~ .8	1.15	----
		E-W-24°	.78	.76	.84	.82	.86	.88	.88	~ .7	.90	----
Sat.	11/27/72	0°.3 N-S	.85	.99	.97	.93	.87	.89	1.03	~ .6	1.10	----
		E-W-31°	.87	.87	.89	.76	.81	.83	.94	----	.94	----
		E-W-52°	.74	.76	.85	.67	.79	.78	.83	~ .8	.78	----
Sat.	11/28/72	0°.4 N-S	.88	.97	.99	.85	.80	.92	1.02	----	1.04	----
		E-W-32°	.81	.75	.78	.84	.76	.78	.82	----	.85	----
		E-W-42°	.80	.84	.68	.72	.80	.75	.80	----	.82	----
Sat.	Mean k	N-S	.88±4	.96±4	.99±2	.92±7	.88±10	.95±8	1.10±10	~ .7	1.10±6	----
	For $\alpha \simeq 0$	E-W<-35°	.84±4	.81±7	.84±7	.80±5	.78±5	.80±3	.88±7	----	.90±6	
		E-W>-35°	.77±4	.80±5	.76±9	.70±4	.80±2	.76±3	.81±3	----	.80±3	

The difference in the variations of k with wavelength for the N-S and E-W traces for Jupiter is readily explained as a result of the absorption variation data presented in paper 1. At almost all wavelengths, the limb darkening is due to the combined effects of the intrinsic limb darkening of the clouds and the center to limb absorption variations of the CH_4 and NH_3 above the clouds. At shorter wavelengths, the contribution of the absorptions to the limb darkening is small (or zero); but with increasing wavelength, the absorptions become stronger so their contribution increases. The absorptions increase towards the limbs for N-S traces, thus the N-S limb darkening must also increase with respect to that of the clouds, i.e. k becomes larger, with increasing wavelengths. Similarly, the absorptions decrease towards the limbs for E-W traces, so the E-W limb darkening must decrease with respect to that of the clouds with increasing wavelengths. Thus, the observed values of k will converge, from opposite side, on the value of k for the clouds alone as shorter wavelengths are approached. Also from paper 1, we know that the absorption variations in the IR are much stronger for the N-S traces then for the E-W traces, resulting in asymmetric, converging curves of k as seen in Figure 4a. This also implies that until the absorption becomes quite strong, i.e. for $\lambda > 1$ μm, the limb darkening of the planet is essentially that of the clouds for E-W traces.

Based on the above discussions and the fact that the N-S and E-W variations in k converge nicely to k = 1.00 at shorter wavelengths and the fact that measurements of the limb darkening at or near the continuum level* at 1.57 μm (paper 1), i.e. of the clouds alone, gives a value of k = 1.0 for N-S and E-W traces, we conclude that $k \equiv 1$ or very nearly so (± 0.01) for the clouds or haze layers over at least the wavelength range of $\lambda\lambda$ 0.60 μm - 1.60 μm.

From Figure 4a and 4b it is clear that the limb darkening of Saturn is significantly different from that of Jupiter in several aspects. First, the N-S and E-W trace values of k do not converge at wavelengths less than 0.7 μm. Secondly,

* The work reported in paper 1 was carried out at a spectral resolution of 300 Å i.e. ~2.5 times the spectral resolution used in the 1.5 μm region for this work (see Table 1). As a result, one of the earlier passbands was nearly free from absorption, so the limb darkening of the clouds alone, at 1.5 μm, was determined from the earlier data.

the values of k for wavelengths where CH_4 absorptions are not important are less than 1 and there appears to be a latitude dependence of k for the E-W traces. Since Jupiter and Saturn seem so similar in most of their properties, it is quite significant that their limb darkening is found to be so different and thus the validity of the data has been checked to verify these findings.

First, because of the comparatively smaller size of Saturn (20" vs 45" for Jupiter) and the presence of the bright rings, the effects of seeing and scattered light on the data are much more serious than for Jupiter. In order to determine the effects of seeing over the ball of the planet on the derived values of k, Dr. J. Pollack computed a series of seeing degraded limb darkening data for us. These computations show that for a worst case of 3" smear (due both to seeing and the finite diameter of our entrance aperature) our derived k's would be ~ 0.05 too high but within the error of our measurements. However, this correction to the derived k's would make the difference between the Jovian and Saturnian limb darkening even greater than observed. This same seeing smear would also bias the E-W limb darkening curves as a function of latitude, in that the higher latitude k's would be biased higher than the lower latitude k's; that is, in the direction opposite to the observed changes of k with latitude. Thus, the real differences in the k's for high and low latitudes would be greater than the observed differences if seeing smear of the ball were the only possible cause of error.

The effects of the rings on the data are, qualitatively, as follows: Because of the geometry, the presence of the rings would tend to increase k for N-S traces, i.e. move it closer to Jovian limb darkening, and decrease k for E-W traces, more so for high latitudes than for low latitudes (this is the sense of the observed differences). However, since at 1.24 μm the rings are brighter than the planet, the above effects would be maximized at this wavelength. Our data does not seem to show such an enhancement at 1.24 μm and so we conclude that the rings have also not seriously contaminated the data (i.e. such errors are on the order of or less than the observed uncertainties).

Thus, the combined effects of the rings and seeing smear of the ball tend to increase k for N-S traces and tend to cancel each other on E-W traces. As a result, we conclude that the above noted differences between the Jovian and Saturnian limb darkening are real.

Based on Figure 4b and the above discussion, it is apparent that unlike the Jovian clouds, the Saturnian clouds do not behave like Lambertian reflecting layers. We conclude that the clouds have values of k in the range of 0.75 to 0.90 for the following reasons. First, at $\lambda < 0.7$ μm, the derived k's are essentially those for the clouds alone since there is little CH_4 absorption at these wavelengths. Secondly, at $\lambda > 1.2$ μm, the CH_4 absorptions are completely or nearly saturated and so the brightness variations over the disk are those due mainly to the clouds. In fact, the 1.55 μm passband is completely clear of the CH_4 absorption and so the k's for $\lambda > 1.2$ μm must also be essentially those for the clouds alone. At intermediate wavelengths (0.7 μm $< \lambda < 1.2$ μm) the CH_4 absorption are not saturated and thus can effect the limb darkening, depending on the absorption variations over the disk (Teifel, 1969). Thus we can use the k's derived for λ = 0.54, 0.64, 1.24 and 1.55 μm, to derive the values of k for the clouds at low latitudes and high latitudes. In doing so, we note that for both sets of data, $\bar{k}$ at $\lambda\lambda$ 1.24 - 1.55 μm is greater than $\bar{k}$ at $\lambda\lambda$ 0.59 - 0.65 μm. However, these differences are on the order of or less than the uncertainties of the observed k's, so we do not consider them to be significant. Thus, we assume k is approximately constant with wavelength and derive values of $k \tilde{=} 0.85 \pm .05$ for southern latitudes less than 35° and $k \tilde{=} 0.80 \pm .05$ for southern latitudes greater than 35° for Saturn cloud limb darkening.

V. SPECTRAL ALBEDOES OF JUPITER AND SATURN

The photometric data obtained for each point on Jupiter and Saturn are converted into geometric albedoes via the observed values of k (Table 2) and the procedures discussed in Section III. The geometric albedoes for the belts, zones, etc. observed are given in Figures 5 and 6 for Jupiter and Saturn respectively, as a function of latitude for all wavelengths observed except λ = 1.44 μm and 1.99 μm for the reasons discussed in the note on page 6. In addition, Figures 7 and 8 give the geometric albedoes for representative features of Jupiter and Saturn as a function

of wavelength. These figures include, for comparison purposes, the geometric albedoes of the planets as derived from full disk photometry (Irvine et al. 1968 and Newburn and Gulkis 1971). The photometric data are superimposed on schematic representation of the spectrum of each planet in order for the reader to assess the effects of the CH_4 and NH_3 absorption on the observed geometric albedoes. Discussion of the normalization of the spectrum to the photometric data is given in Section VI.

There are four points to be made regarding the albedoes. First, there are significant differences between the two sets of Jupiter data represented in Figure 5, which are of course not surprising since the two sets are separated by 13 months of time. Previous long term observations of Jupiter (e.g. Irvine et al. 1968) show time dependent variations of 10% or greater in its geometric albedo. It is expected that individual features will show even greater time dependent variations than does the full disk. Thus, the data presented in Figures 5-8 has at least a 10% time dependent bias and that it is our opinion, that the current Jupiter data are on the lower side of the time average mean because of the general dusky appearance of the planet during our observing periods.

Secondly, as is also known from color photography of Jupiter, the relative contrast between the various features varies considerably with wavelength. For example in Figure 5 there are marked changes in the contrast between the South Tropical Zone (STrZ), the Equatorial Region [the Equatorial Zone* (EZ) and the North Equatorial Belt (NEB)] and the Great Red Spot (GRS) with increasing wavelength. These relative changes are in part due to the CH_4 and NH_3 variations over the features as discussed in paper 1.

Thirdly, the geometric albedoes given are not in general the albedoes of the continuum; the effects of the absorption due to CH_4 and NH_3 on the true albedoes are discussed in Section VI.

---

* During both years, the EZ was nearly as dark as the NEB and so the entire equatorial region looked like a very broad, dark band which we refer to simply as the Equatorial Region (ER).

Finally, because of the finite width of the entrance aperture, it was not always possible to measure a completely uniform area. Thus, the albedoes derived for small features such as the South Temperate Zone (STZ), South Temperate Belt (STB) and for the edges of the polar regions, which often contain faint zones and belts, are biased by their surroundings.

In general the above argument also applied to the Saturn spectral albedoes, with one notable exception. As is shown in Figure 6, the contrast between the various features of Saturn does not appear to vary with wavelength. At all eight wavelengths Saturn has a relatively uniform albedo as a function of latitude except for a 10% dip at 30^{o} south latitude.

Also, the observed geometric albedoes of Saturn are higher than those of Jupiter. At wavelengths greater than 1 μm, this is in part due to the fact the NH_3 absorptions are absent on Saturn and so the IR windows are more open for Saturn than for Jupiter (compare Figures 7 and 8). At shorter wavelengths, Saturn is 10-20% brighter than Jupiter. This difference is probably, in part due to the time dependent variations mentioned above, but also may in part be time independent.

We also note that the normalized spectral curves of Jupiter and Saturn (Figures 7 and 8) are very similar. Thus, we conclude that the color and composition of the Jovian and Saturnian cloud layers are very nearly identical.

VI. SCATTERING PROPERTIES OF THE JOVIAN CLOUD LAYERS

The limb darkening data and geometric albedoes derived in the previous section can be used to derive new information regarding the nature and physical properties of the Jovian cloud layers. Following the discussions of Harris (1961) it is apparent that, while the Jovian cloud layer particles do not behave as isotropic scatters, an asymmetric scattering function, such as Euler's function, might be applicable for representing the scattering properties of Jupiter when limb darkening

data and geometric albedoes are both available. This scattering function has the form

$$P(\cos\theta) = \tilde{\omega}_0 (1 + a \cos\theta) \qquad (12)$$

where $\tilde{\omega}_0$ is the single scattering albedo, θ is the scattering angle and $\underline{a}$ is a dimensionless coefficient which varies between 1 and -1. When $\underline{a}$ is 1 the particle scatters predominately forward, when a = 0 the particle scatters isotropically, and when a = -1 the particle scatters predominately backwards. Harris has computed for a few cases the values of x and G, values which we need to define $\tilde{\omega}_0$ and α (see Harris 1961, Table 23). Similarly, Horak and Little (1965) have computed the brightness over the disk of hypothetical planets for several additional cases, over a wide range of phase angles. However, these sets of theoretical data are insufficient for the purposes of this paper. Hence, additional values of x and G were computed for the range of $0 < \tilde{\omega}_0 \leq 1$ and $-1 \leq a \leq 1$ for zero degrees phase angle (α). Following Chandrasekhar (1950) the brightness at a point on a disk whose cloud particles scatter according to the Euler function is, at zero optical depth,

$$I(\mu, \varphi, \mu_0, \varphi_0) = \frac{\mu_0 \tilde{\omega}_0 F}{4(\mu + \mu_0)} \left\{ \psi(\mu)\,\psi(\mu_0) - a\,\theta(\mu)\,\theta(\mu_0) + a \left[(1-\mu^2)^{1/2} H^{(1)}(\mu)\right] \left[(1-\mu_0^2)^{1/2} H^{(1)}(\mu_0)\right] \cos(\varphi_0 - \varphi) \right\} \qquad (13)$$

where, μ is cos i, μ_0 is cos e, φ the azmuthial angle of the point from the sub-solar point, φ_0 the azmuthial angle of the point from the sub-earth point; $\psi(\mu)$, $\psi(\mu_0)$, $\theta(\mu)$, $\theta(\mu_0)$ $H^{(1)}(\mu)$ and $H^{(1)}(\mu_0)$ are tabulated in Chandrasekhar (1950).

However, at $\alpha = 0$, $\mu = \mu_0$ and $\cos(\varphi_0 - \varphi) = -1$, so equation 13 becomes

$$I(\mu) = \frac{\tilde{\omega}_0 F}{8} \left\{ \psi^2(\mu) - a\,\theta^2(\mu) - a\,(1-\mu^2)\,H^{(1)^2}(\mu) \right\} \qquad (14)$$

Thus, by (3) and (14) x is

$$x = \frac{2I_{(0.5)}}{I_{(0.1)}} = \frac{2\left\{\psi^2_{(0.5)} - a\,\theta^2_{(0.5)} - 0.75\,a\,H^{(1)^2}_{(0.5)}\right\}}{\psi^2_{(1)} - a\,\theta^2_{(1)}} \tag{15}$$

Equation (5) can then be used to express the calculated values of x in terms of k, the Minnaert limb darkening coefficient. Rewriting equation (5) we have

$$k = \frac{0.693 - \ln(\frac{x}{2})}{1.386} \tag{16}$$

Also by equations (11) and (14) the geometric albedo is given by

$$G = \frac{2}{2k+1} \quad \frac{\tilde{\omega}_0}{8}\left(\psi^2_{(1)} - a\,\theta^2_{(1)}\right) \tag{17}$$

Using equations (15), (16) and 17), values of k and G were computed and are presented in Figures 9, from which values of $\tilde{\omega}_0$ and a for each belt, zone or spot observed can be derived given the geometric albedoes of the clouds alone.

As discussed in Section V, the albedoes given in Figures 6 and 7 for various areas on Jupiter are the observed geometric albedoes. These values are corrected for the NH_3 and CH_4 absorption in the passband of the 10 channel spectrometer as follows. First, using spectrophotometric data on the IR spectrum at the center of the disk of Jupiter (Cruikshank and Binder 1968, 1969 and Woodman, private communication), a filter factor was derived which relates the observed intensity at each each wavelength (except 1.44 and 1.99 μm) to the maximum intensity of the window in which the passband lies. For example (see Figure 7) the maximum of the peak of the 1.5 μm window of Jupiter is found to be brighter than the observed intensity as defined by the 1.55 μm passband by 40%, or the maximum at 0.82 μm is 19% brighter than that observed by the 0.825 μm passband, when the effects of the

absorptions are considered. Using these filter factors (see Table 3) and the photometric data fiven in Figure 5 were used to define the normalized Jovian spectrophotometric curve as shown in Figure 7.

Secondly, the peak of the windows of Jupiter beyond 1.1 μm do not lie at the continuum level and so, using laboratory data (Cruikshank and Binder 1968) an additional coefficient was derived (see Table 3) which, when multiplied by the observed geometric albedo and the filter factor, gives the geometric albedo of the cloud layer. It is recognized that these filter factors, estimates of continuum level factors are difficult to make, especially at longer wavelength where the absorptions are very strong. Thus, the final values derived for the geometric albedoes of the clouds are most probably in error by a few percent at short wavelengths and up to 10% or perhaps more at longer wavelengths.

With these cautionary remarks in mind, values of G for the cloud layer of the various belts, zones or the Red Spot can be derived using the data in Table 3 and the values of the observed G in Figure 5. Using these final values of G and a value of $k \equiv 1$ for Jupiter, $\tilde{\omega}_0$ and $\underline{a}$ can be determined for the Euler function for each feature from Figure 9.

Figures 10a and 10b give the values derived by this procedure for the STrZ and the dark EZ of Jupiter. From Figures 10a and 10b, it is apparent that the Jovian cloud layers show a strong wavelength dependency in their scattering properties. First, after an initial rise between 0.60 and 0.65 μm, $\tilde{\omega}_0$ drops off rapidly with increasing wavelength to 1.2 μm where $\tilde{\omega}_0$ then apparently begins to increase moderately again. This behavior is not that expected for a uniform population of white scatters, since in this case $\tilde{\omega}_0$ would show a continual increase with increasing wavelength. However, since the cloud particles are most probably NH_3 crystals, it is likely that the decrease of $\tilde{\omega}_0$ with wavelength beyond 0.65 μm is due to the solid state absorptions of the NH_3 crystals, absorption which should increase in strength in the regions beyond 0.65 μm and hence darken the particles. Alternatively, it is possible that at the shorter wavelength, we are measuring the scattering properties of an upper cloud layer (Clements and Tomasko, private

TABLE 3

FILTER AND CONTINUUM LEVEL FACTORS

	Jupiter	Jupiter	Saturn
		Continuum Level	
λ(μm)	Filter Factor	Factor	Filter Factor
0.59	1.00	1.00	1.00
0.64	1.03	1.00	1.06
0.72	1.29	1.00	1.54
0.82	1.19	1.00	1.29
0.96	1.45	1.00	1.55
1.08	1.30	1.00	1.15
1.24	1.51	1.13	1.31
1.55	1.40	1.22	1.00

communication). With increasing wavelength, the scattering efficiency of this upper layer may become increasingly smaller and so the light reaches a second cloud layer, whose $\tilde{\omega}_0$ is less than that of the upper layer. Thus we might be seeing the combined effects of two different populations of scatters at different levels in the atmosphere.

Figure 10b shows that, at the shorter wavelength, the cloud layers are moderately forward scattering and that as longer wavelengths are reached, the scattering becomes more and more forward. Using the data presented in Figures 10a and 10b, we find that

$$0.960\ (1 + 0.85 \cos\theta) \leq p\ (\cos\theta) \leq 0.994\ (1 + 0.42 \cos\theta) \tag{18}$$

for the general range of G over all observed wavelengths. The maximum and minimum values, based on our present data are

$$p\ (\cos\theta) = 0.997\ (1 + 0.30 \cos\ \theta) \tag{19}$$

for $\lambda = 0.64\ \mu$m in the STZ and

$$p\ (\cos\theta) = 0.945\ (1 + 0.94 \cos\theta) \tag{20}$$

for $\lambda = 1.55\ \mu$m in the NPR. If it is assumed that the maximum time dependent geometric albedoes are 10% higher than our value, then at $\lambda = 0.64\ \mu$m, one would have Gmax $\sim$ 0.64 and from Figure 9

$$p\ (\cos\theta) = 0.998\ (1 + 0.20 \cos\theta) \tag{21}$$

Thus, even for the most favorable case, we find that a conservative, isotropic scattering model is not valid for Jupiter and hence at least an asymmetric scattering function, like Euler's function, is needed. While the more general form

$$p\ (\cos\theta) = 1 + \tilde{\omega}_1 P_2\ (\cos\theta) + \tilde{\omega}_2 P_2\ (\cos\theta) \tag{22}$$

may ultimately be required to fit Jovian scattering data (i.e. photometric data taken from spacecrafts at large phase angles or absorption line profiles taken at the extreme edge of the disk), the two parameter Euler function adequately fits the available data.

VII. SCATTERING PROPERTIES OF THE SATURNIAN CLOUD LAYERS

In general, the Saturn data were treated in the same way as were the Jupiter data in that the observed geometric albedoes were converted into continuum albedoes using filter factors (as given in Table 3) derived from IR spectral data of Saturn (Johnson, 1970 and Younkin, private communication). These data were used to derive the normalized Saturn spectral reflectivity curve given in Figure 8. Figure 10 gives the ranges of $\tilde{\omega}_0$ and $\underline{a}$ for the Euler function, based on derived ranges of k and G for Saturn.

From Figure 11 it is apparent that for $k = 0.80$ and 0.85 and $48\% \leq G \leq 68\%$, (as derived from Figure 6 and Table 3) the Euler scattering function does not satisfactorily represent the scattering properties of Saturn. First, the function fails to give albedoes as high as those observed around 0.7 μm if, as is observed for high latitudes, k is less than about 0.85. This problem may not be fatal, because of the possible biases in both G and k. If Gmax were only $\sim 60\%$ and kmax ~ 0.8, then the Euler function would satisfy all the data. However, at all observed wavelengths, $-1 \leq a \leq -0.3$, so the function is predominately back scattering. This seems to be inconsistant with the general behavior of scattering particles. As a result, it is possible that a different function is needed to properly model the Saturnian cloud layer scattering, or that simple scattering from uniform cloud layers does not apply in this case. For example, Schoenberg (1925) has shown that at $\alpha = 0$ a Lambertian sphere whose surface is covered with small cones or hemispheres (which also reflect according to Lamberts Law) has values of $0.7 \leq k \leq 0.85$. The exact value of k depends on the shape of the proturbences and their relative spacings. Based on (1) the similarity of the derived values of k for Saturn's clouds and those derived by Schoenberg, and (2) the similarity of the geometry of cumulus clouds and to that of the cones and hemispheres used in the Schoenberg calculations, we suggest that Squires' cumulus cloud model for Jupiter (1957) may actually apply to Saturn rather than Jupiter. If this is the case, then the cloud particles of Saturn may individually behave like those of Jupiter [as is indicated in part by their similar reflectivity profiles (Section V)] but the macroscopic

"topography" of the Saturnian clouds cause the limb darkening of the two planets to differ. Also, the latitude dependence of k for Saturn may be due to changes in the geometry and spacing of the cumulus clouds with increasing latitude.

VIII. SUMMARY

Spectrophotometric data taken over the wavelength range λλ 0.6 - 2.0 μm are used to show the general applicability of the Minnaert function for representing Jovian and Saturnian limb darkening. These data also indicate that the observed wavelength dependent variations of the limb darkening of both planets is really explained as the combined effects of the intrinsic limb darkening of the clouds and the center to limb absorption variations of NH_3 and/or CH_4. Also the limb darkening of the clouds of Jupiter is significantly different from that of the Saturnian clouds. The value of k for the Jovian clouds is found to be 1.0 for all parts of disk, while k for the Saturnian clouds is found to be latitude dependent and to be in the range of 0.75 to 0.90.

Geometric albedoes are derived for various features of Jupiter. These albedoes coupled with the limb darkening data are used to derive $\tilde{\omega}_0$ and $\underline{a}$ for the Euler scattering function. As a result, we show that isotropic scattering is not valid for Jupiter, but that at least an asymmetric scattering function, such as Euler's, is needed to fit the valuable data. The derived values show that $\tilde{\omega}_0$ decreases with increasing wavelength. This decrease may be due to the color of the NH_3 crystals which probably make up the clouds.

It is also shown that the Euler function does not adequately fit the Saturn data. As a result, it is suggested that Squires' (1957) cumulus cloud model may apply to Saturn.

This research was sponsored by the National Aeronautics and Space Administration under contract NASW - 2363.

REFERENCES

Binder, A.B. 1972, Astron. J., 77, 93.

Binder, A.B., and Jones, J.C. 1969, Proceedings of the Sixth International Symposium on Remote Sensing of Environment (University of Michigan, Ann Arbor), p. 1305.

Binder, A.B., and Jones, J.C. 1972, J. Geophys. Res., 77, 3005.

Chandrasekhar, S.1950, Radiative Transfer (Oxford: Clarendon Press).

Cruikshank, D.P., and Binder, A.B. 1968, Commun. Lunar Planet. Lab., 6, 275.

_____1969, Astrophys. Space Sci., 3, 347.

Harris, D.L. 1961, Planets and Satellites, Vol. III of The Solar System, G.P. Kuiper and B.M. Middlehurst, Eds. (University of Chicago Press, Chicago), p. 321.

Hess, S.L. 1953, Astrophys. J., 118, 151.

Horak, H.G. and Little, S.J. 1965, Astrophys. J. Supp. Ser., No. 101, 373.

Irvine, W.M., Simon, T., Mensel, D.H., Pikoos, C., and Young, A.T. 1968, Astron. J., 73, 807.

Johnson, H.L. 1965, Commun. Lunar Planet. Lab., 4, 99.

Johnson, H.L., Mitchell, R.I., Iriarte, B., and Wisniewski, W.Z.,1966, Commun. Lunar Planet. Lab., 4, 99.

Newburn, Jr., R.L., and Gulkis, S. 1971, JPL Tech. Rpt. 32-1529, (Pasadena: Calif. Inst. Tech).

Moroz, V.I., and Cruikshank, D.P. 1969, J. Atmos. Sci., 26, 865.

Münch, G., and Younkin, R.L. 1964, Astron. J., 69, 553 (abstract).

Owen, T., and Mason, H.P. 1969, J. Atmos. Sci., 26, 870.

Schoenberg, E. 1925, Acta Societatis Scientiarum Fennicoe, 50, 6.

Squires, P. 1957, Astrophys. J., 126, 185.

Teifel, V. G. 1969, J. Atmos. Sci., 26, 854.

Young, A.T. 1970, Applied Optics, 9, 1874.

CAPTIONS

Fig. 1. Plots of log (B_s . cos e) versus log (cos i . cos e) for representative E-W and N-S traces over the disk of Jupiter.

Fig. 2. Plots of log (B_s . cos e) versus log (cos i . cos e) for representative E-W and N-S traces over the disk of Saturn.

Fig. 3. Plots of log (B_s . cos e) versus log (cos i . cos e) for theoretical planets with thick cloud layers whose particles scatter according to Euler's function. The bottom three curves are for $\alpha = 0$. The upper most curve is for $\alpha = 10^{o}$.

Fig. 4a - 4b. Plots of the observed values of k for Jupiter and Saturn respectively versus wavelength and wavenumber. In both figures, the filled circles represent the k's for N-S traces and the open symbols represent the k's for E-W traces. Further, in Fig. 4b, the open circles are the k's derived for E-W traces, for southern latitudes less than 35^{o} and the open squares on the k's derived for E-W traces for southern latitudes greater than 35^{o}.

Fig. 5. Plots of the geometric albedo versus zenographic latitude for the areas observed on the central meridian of Jupiter. The open symbols are for visually bright features and filled symbols are for visually dark features. The circles (open and filled) are data taken on May 11, 1971 and the triangles (open and filled) are data taken on June 25, 1972. The features observed are identified at the top. The wavelength is given on each graph.

Fig. 6. Plots of the geometric albedo versus Saturnographic latitude for the areas observed on the central meridian of Saturn. The open circles are data taken on November 25, 1972 and the filled circles are data taken on November 27, 1972. The wavelength is given on each graph.

Fig. 7. Plot of a geometric albedo versus wavelength for the STrZ of Jupiter. The curve is the normalized spectral reflectivity curve of Jupiter. The crosses are the new data presented in the paper (the width of the crossbar is equal to the passband width of that detector). The filled circles are data presented by Newburn, Jr. and Gulkis (1971) and the open squares of data presented by Irvine et al. (1968).

Fig. 8. Plot of geometric albedo versus wavelength for Saturn (average of all points). The curve is the normalized spectral reflectivity curve of Saturn. The crosses are the new data presented in this paper (the width of the crossbar is equal to the passband width of that detector). The filled circles are data presented by Newburn, Jr. and Gulkis (1971).

Fig. 9. Plot of k and G as functions of $\tilde{\omega}_0$ and $\underline{a}$. The ranges of the variables cover the ranges observed for the Jovian cloud layers. The values of k are identified on the right side of the graphs. For Jupiter $k \equiv 1$, but values of $k = 1.03$ and 0.97 are also given for comparison purposes. The values of G of each line is given within the graph.

Fig. 10a - 10b. Plots of $\tilde{\omega}_0$ versus wavelength and $\underline{a}$ versus wavelength, respectively, for the Jovian cloud layers. The open circles are for the STrZ and the filled circles are for the ER.

Fig. 11. Plot of k and G as functions of $\tilde{\omega}_0$ and $\underline{a}$. The ranges of the variables cover the ranges observed for the Saturn cloud layers. The values of k are identified on the right side of the graph. The values of G of each line is given within the graph.

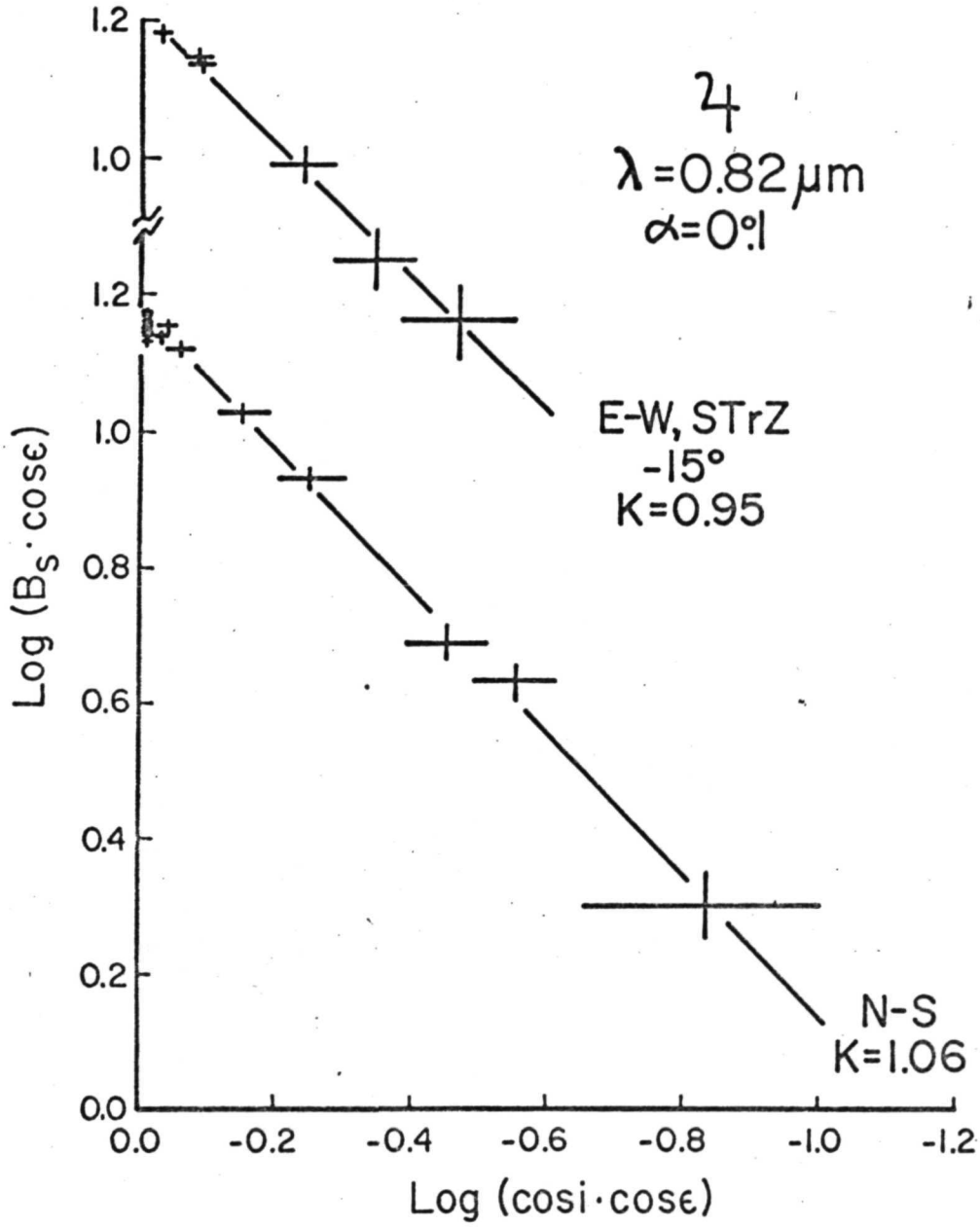
4
λ=0.82μm
α=0°1
E-W, STrZ
-15°
K=0.95
N-S
K=1.06
Log (Bs · cosε)
Log (cosi · cosε)
1.2
1.0
1.2
1.0
0.8
0.6
0.4
0.2
0.0
0.0
-0.2
-0.4
-0.6
-0.8
-1.0
-1.2

FIGURE 1

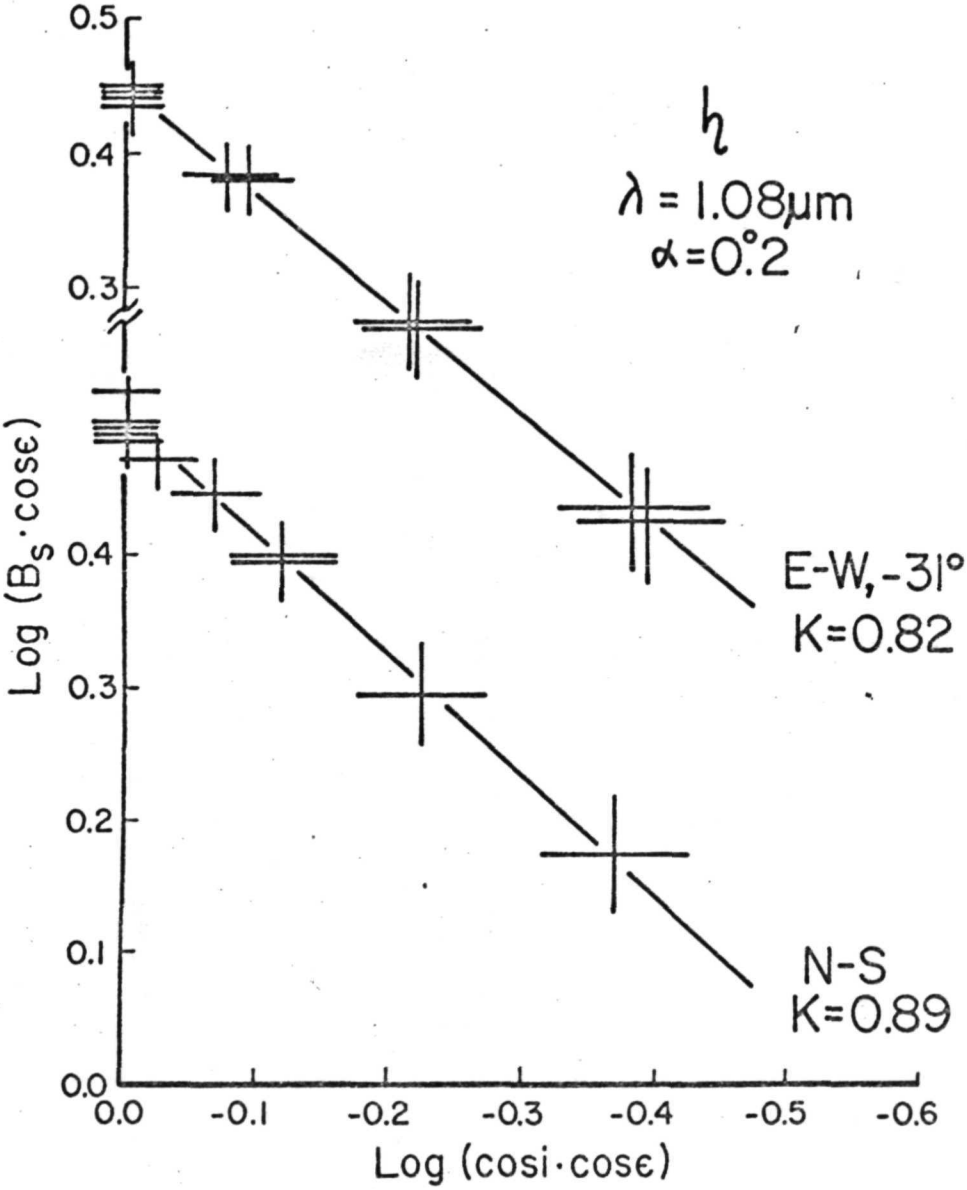
h
λ = 1.08μm
α=0°.2
E-W, -31°
K=0.82
N-S
K=0.89
Log (Bs·cosε)
Log (cosi·cosε)
0.5
0.4
0.3
0.4
0.3
0.2
0.1
0.0
0.0
-0.1
-0.2
-0.3
-0.4
-0.5
-0.6

FIGURE 2

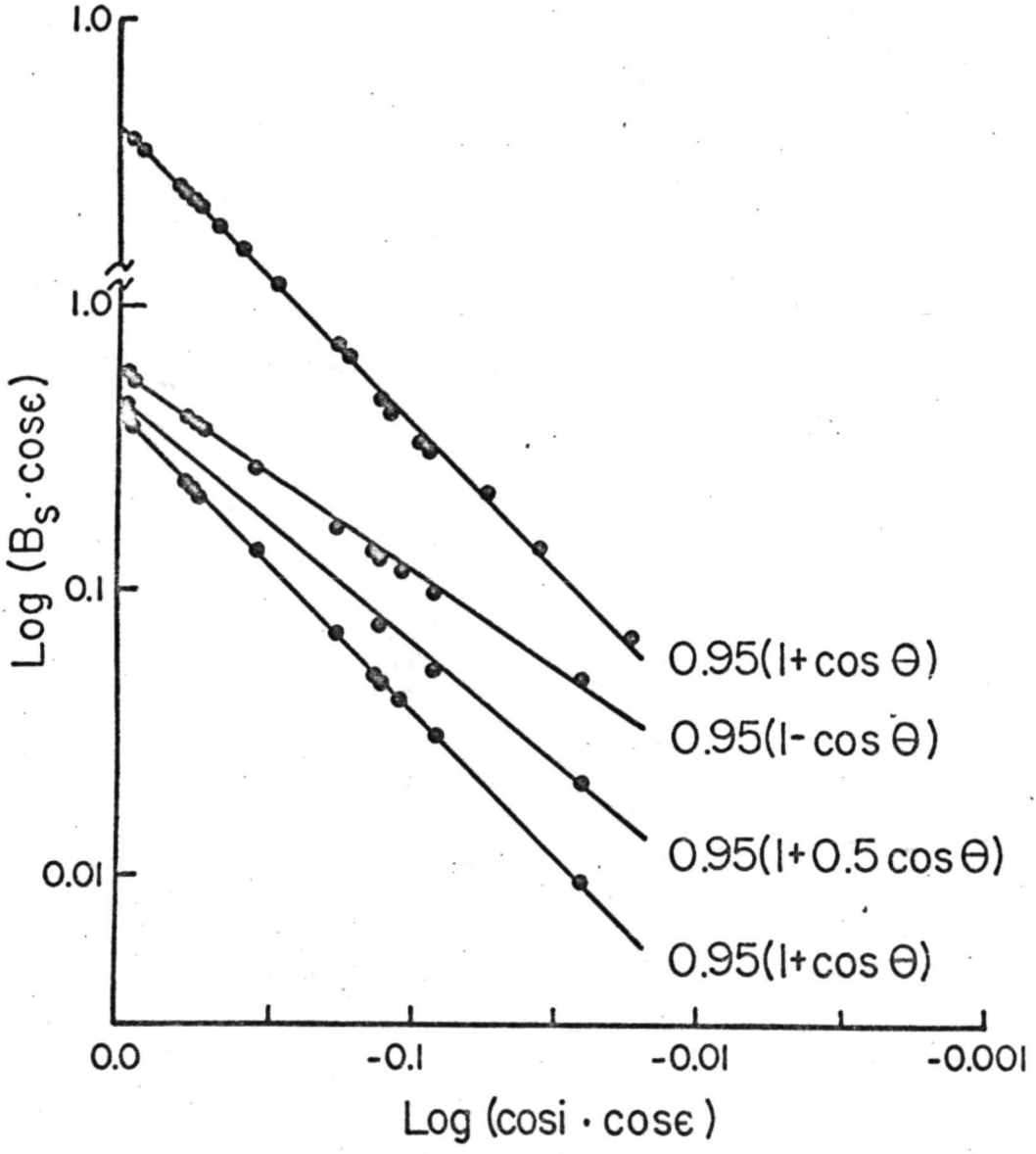
1.0
1.0
0.1
0.01
Log ($B_s \cdot \cos\epsilon$)
0.95(1+cos Θ)
0.95(1-cos Θ)
0.95(1+0.5 cos Θ)
0.95(1+cos Θ)
0.0
-0.1
-0.01
-0.001
Log (cosi · cosε)

FIGURE 3

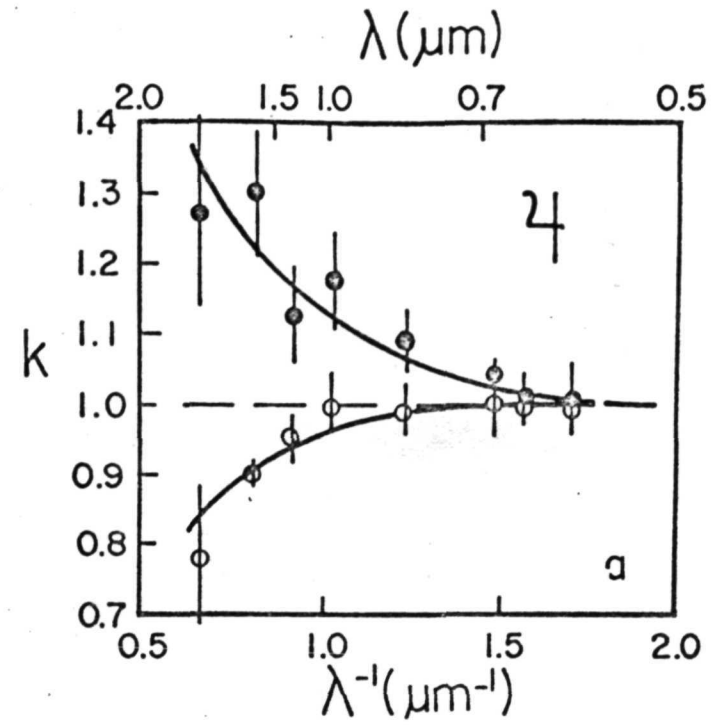
λ (μm)
2.0
1.5
1.0
0.7
0.5
1.4
1.3
1.2
1.1
1.0
0.9
0.8
0.7
k
4
a
0.5
1.0
1.5
2.0
λ⁻¹(μm⁻¹)

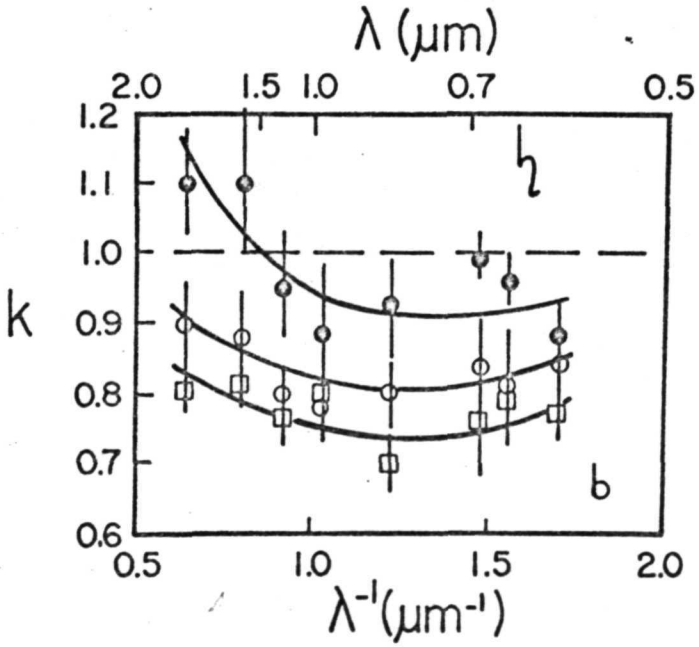
λ (μm)
2.0
1.5
1.0
0.7
0.5
1.2
1.1
1.0
0.9
0.8
0.7
0.6
k
4
b
0.5
1.0
1.5
2.0
λ⁻¹(μm⁻¹)

FIGURE 4a-4b

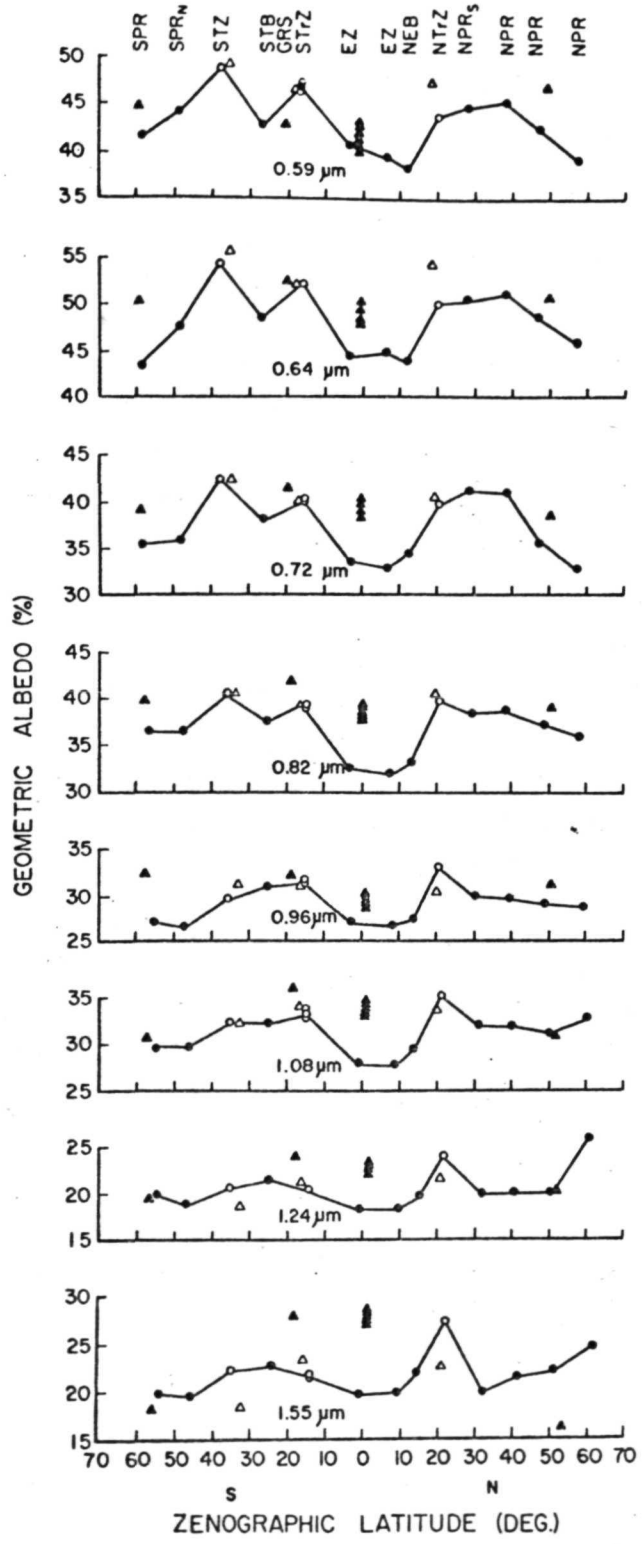
SPR
SPR$_N$
STZ
STB
GRS
STrZ
EZ
EZ
NEB
NTrZ
NPR$_S$
NPR
NPR
NPR
0.59 μm
0.64 μm
0.72 μm
0.82 μm
0.96μm
1.08μm
1.24μm
1.55 μm
GEOMETRIC ALBEDO (%)
70 60 50 40 30 20 10 0 10 20 30 40 50 60 70
S
N
ZENOGRAPHIC LATITUDE (DEG.)

FIGURE 5

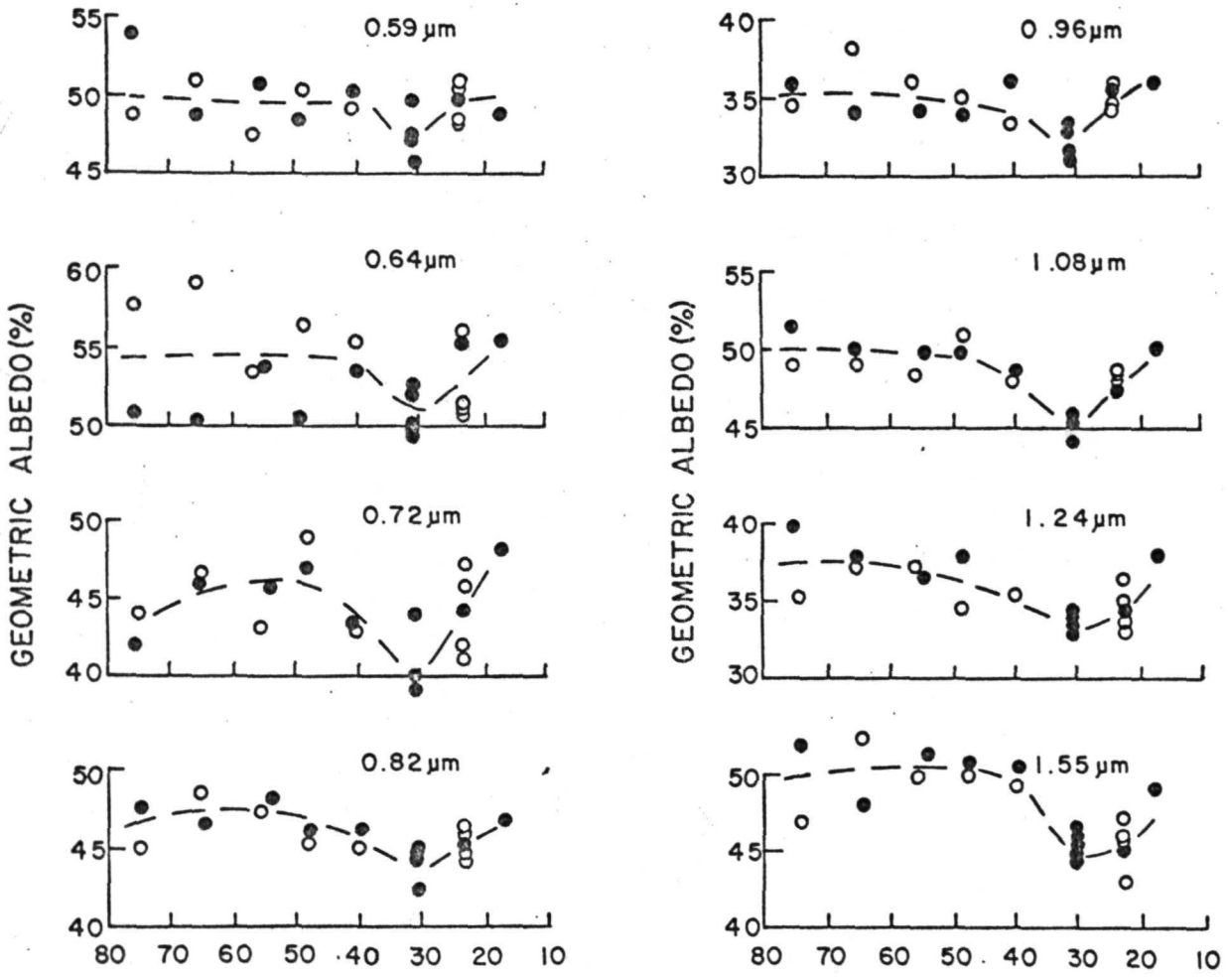
0.59 μm
0.64 μm
0.72 μm
0.82 μm
0.96 μm
1.08 μm
1.24 μm
1.55 μm
GEOMETRIC ALBEDO (%)
GEOMETRIC ALBEDO (%)
SATURNOGRAPHIC LATITUDE (SOUTH, DEG.)
80 70 60 50 40 30 20 10

FIGURE 6

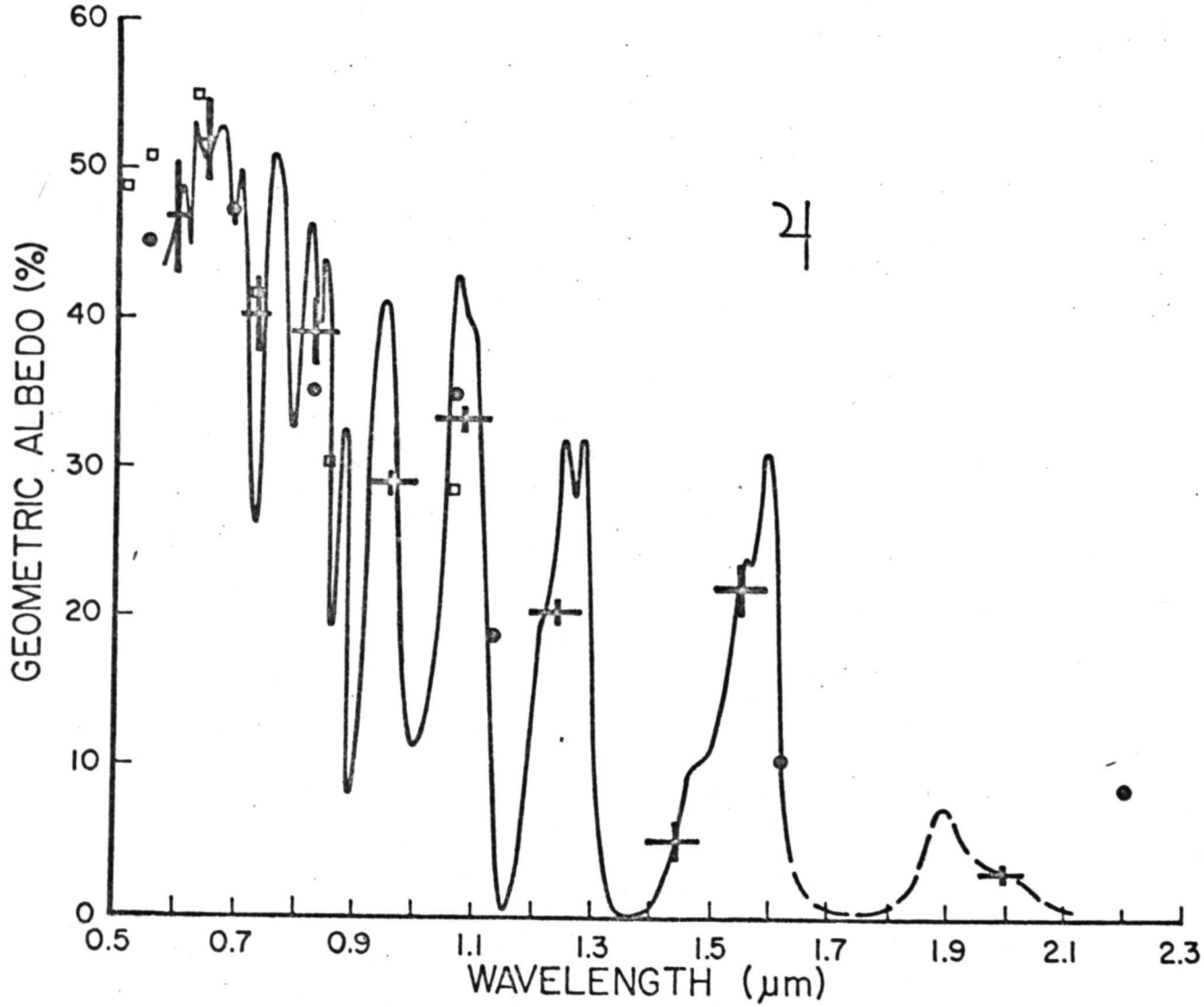
GEOMETRIC ALBEDO (%)
60
50
40
30
20
10
0
0.5
0.7
0.9
1.1
1.3
1.5
1.7
1.9
2.1
2.3
WAVELENGTH (μm)
21

FIGURE 7

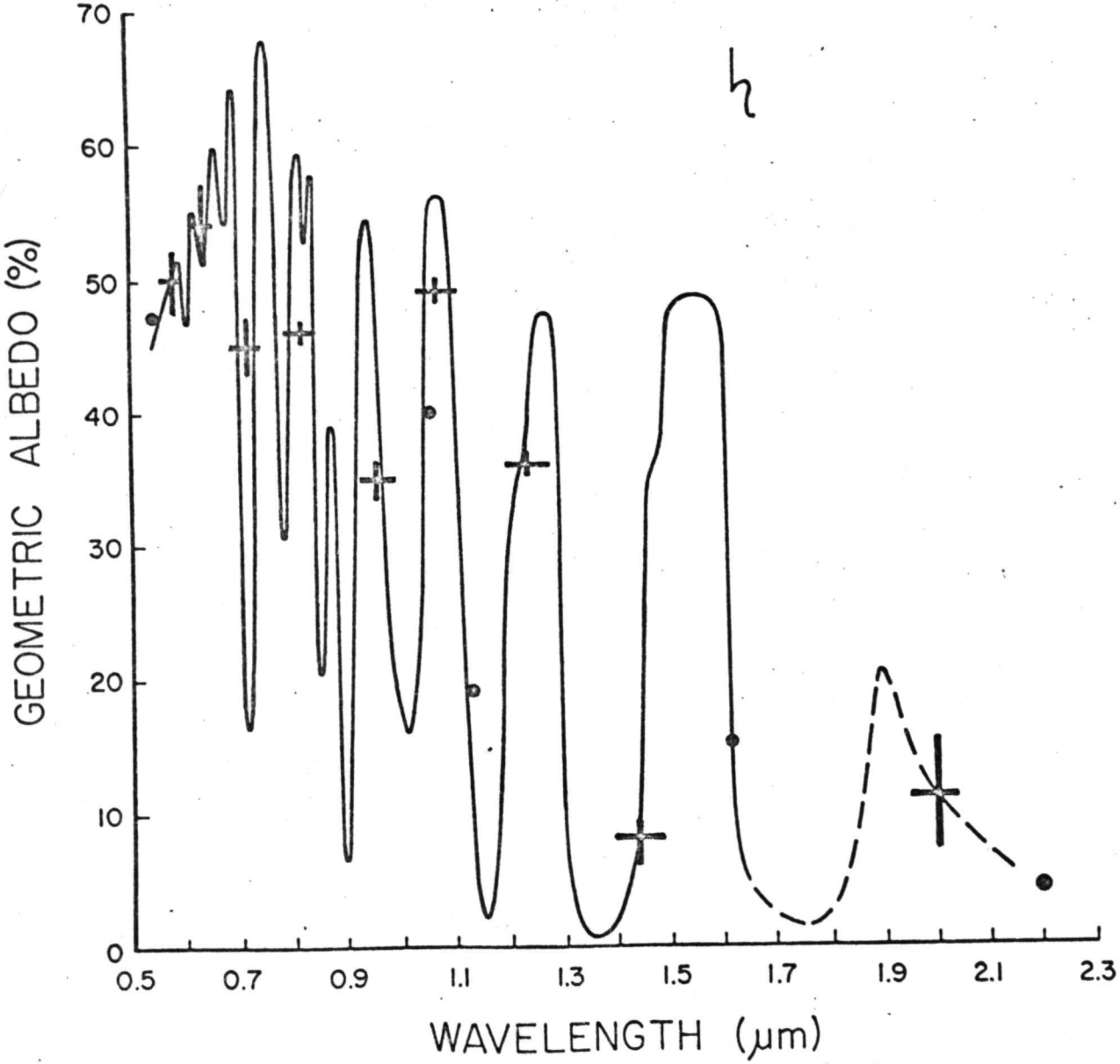
70
60
50
40
30
20
10
0
GEOMETRIC ALBEDO (%)
0.5
0.7
0.9
1.1
1.3
1.5
1.7
1.9
2.1
2.3
WAVELENGTH (μm)
ħ

FIGURE 8

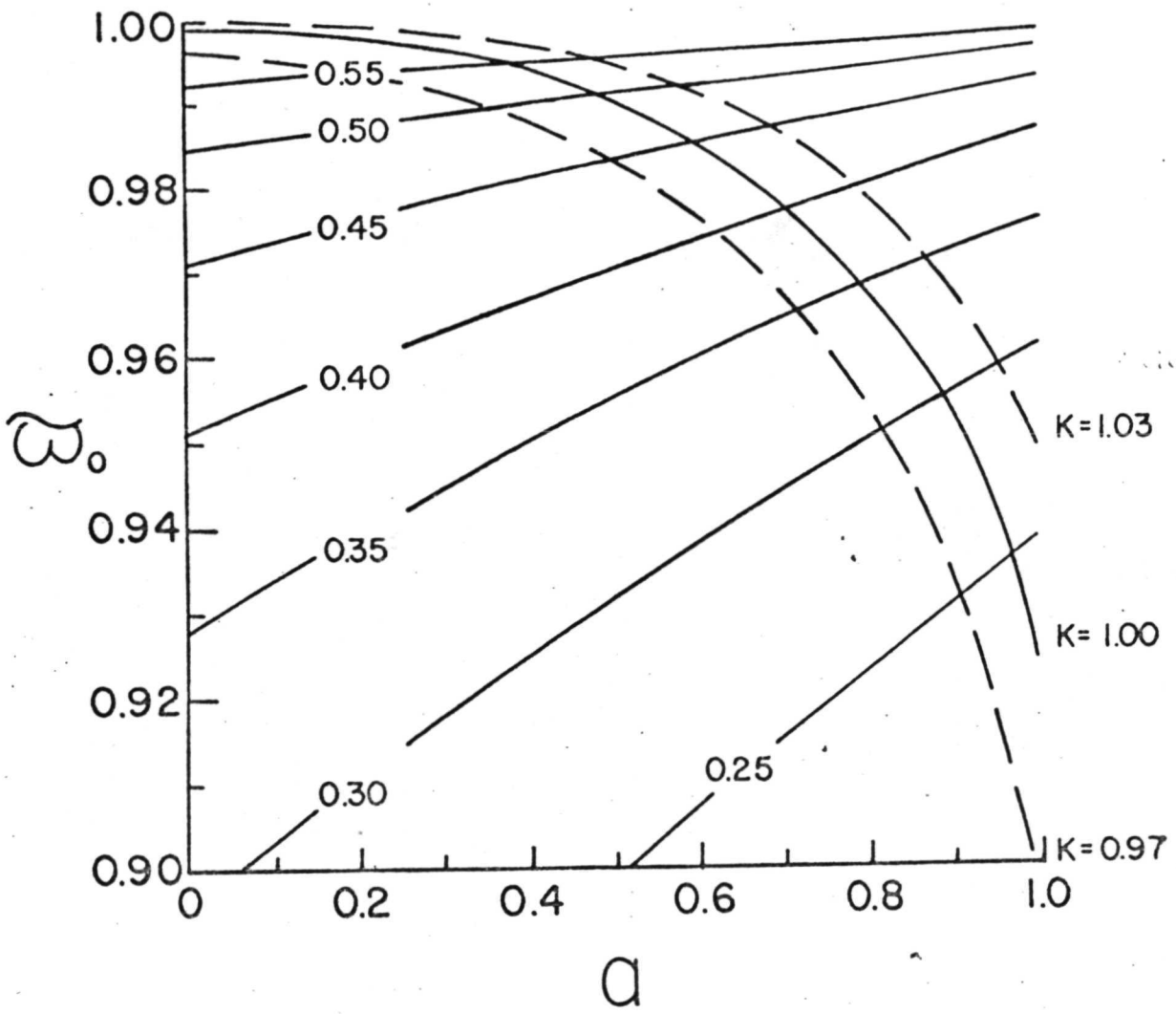
1.00
0.98
0.96
0.94
0.92
0.90
ϖ_o
0.55
0.50
0.45
0.40
0.35
0.30
0.25
K=1.03
K=1.00
K=0.97
0
0.2
0.4
0.6
0.8
1.0
a

FIGURE 9

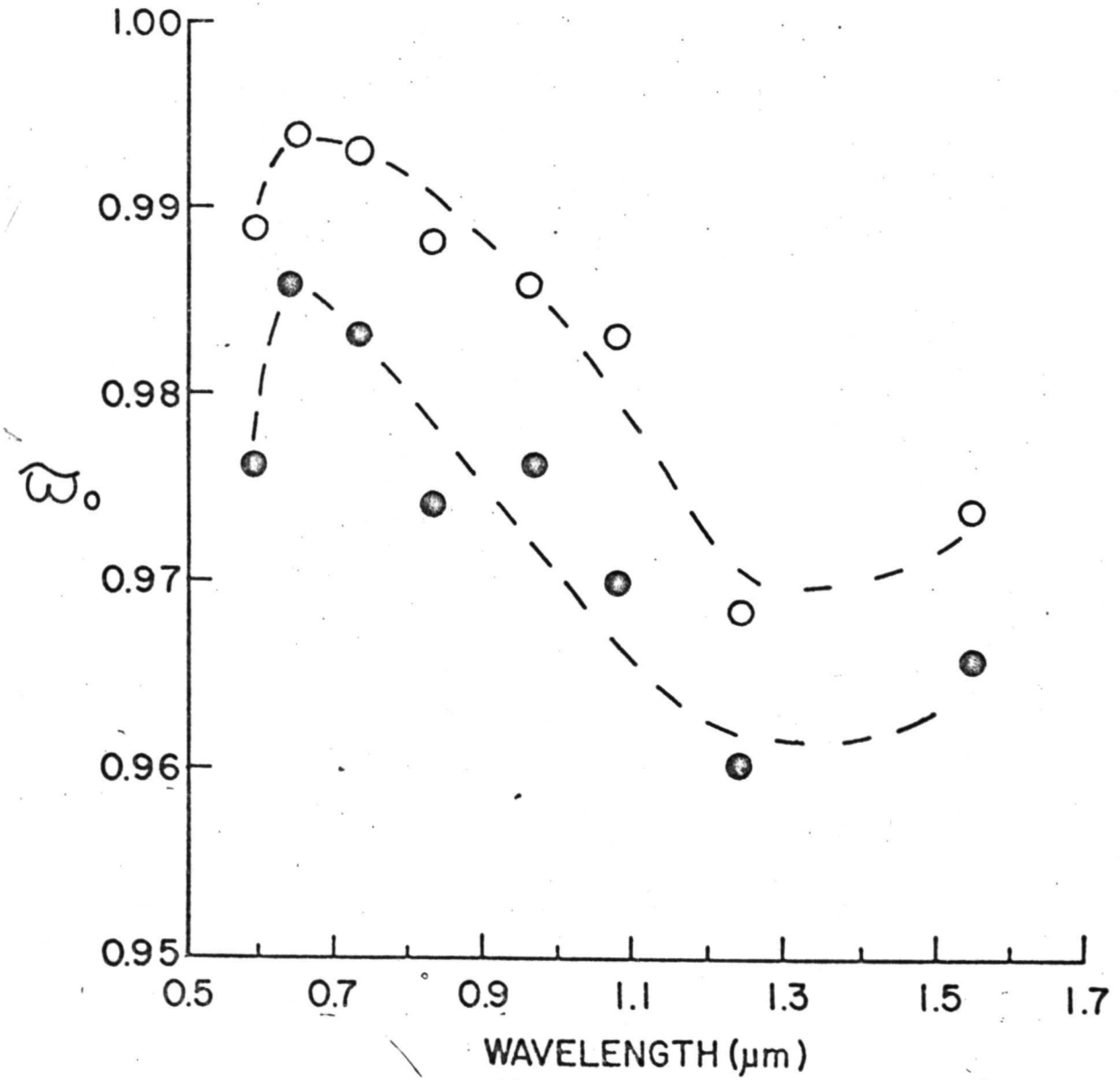
1.00
0.99
0.98
0.97
0.96
0.95
ω_o
0.5
0.7
0.9
1.1
1.3
1.5
1.7
WAVELENGTH (μm)

FIGURE 10a

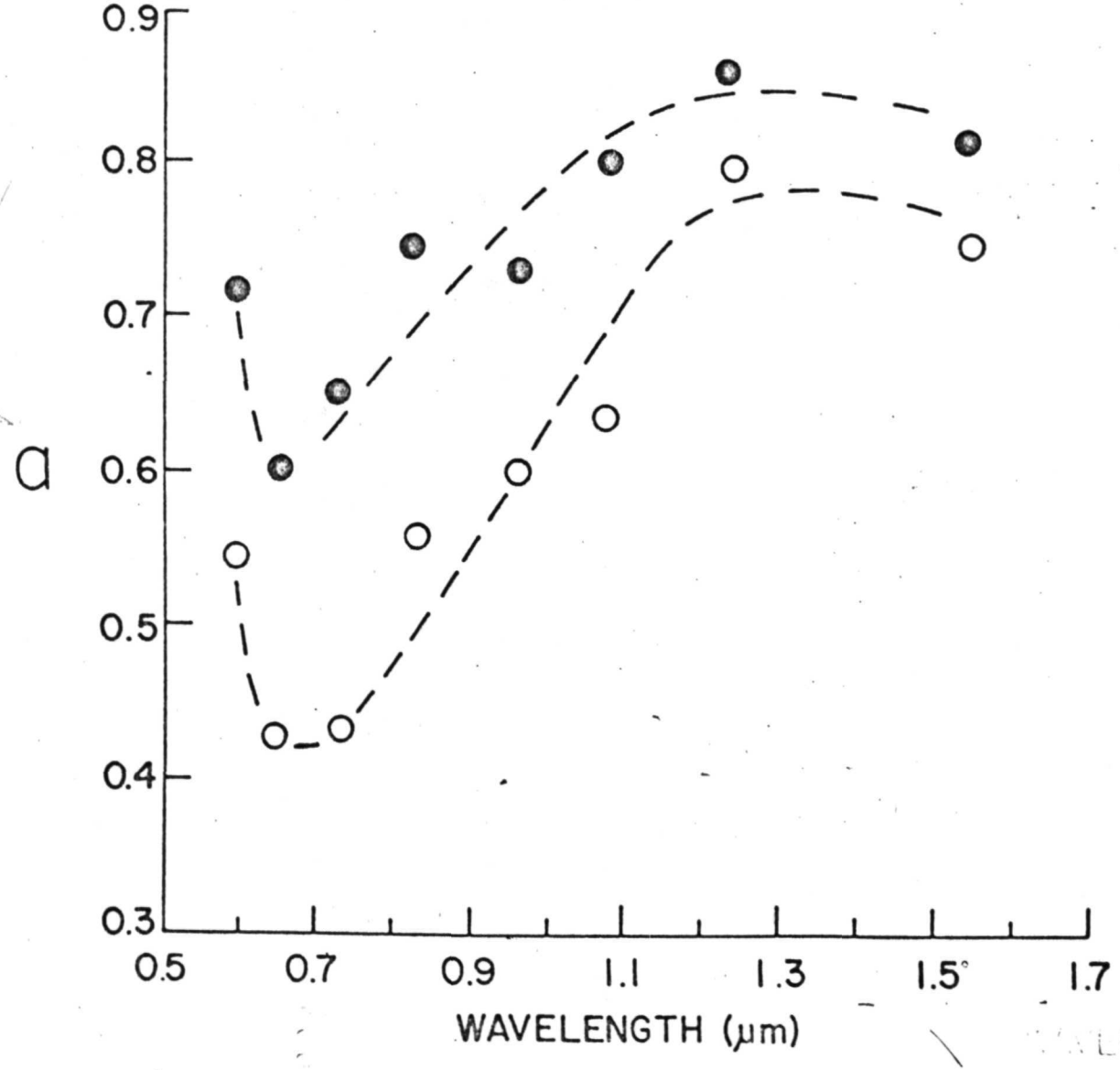

FIGURE 10b

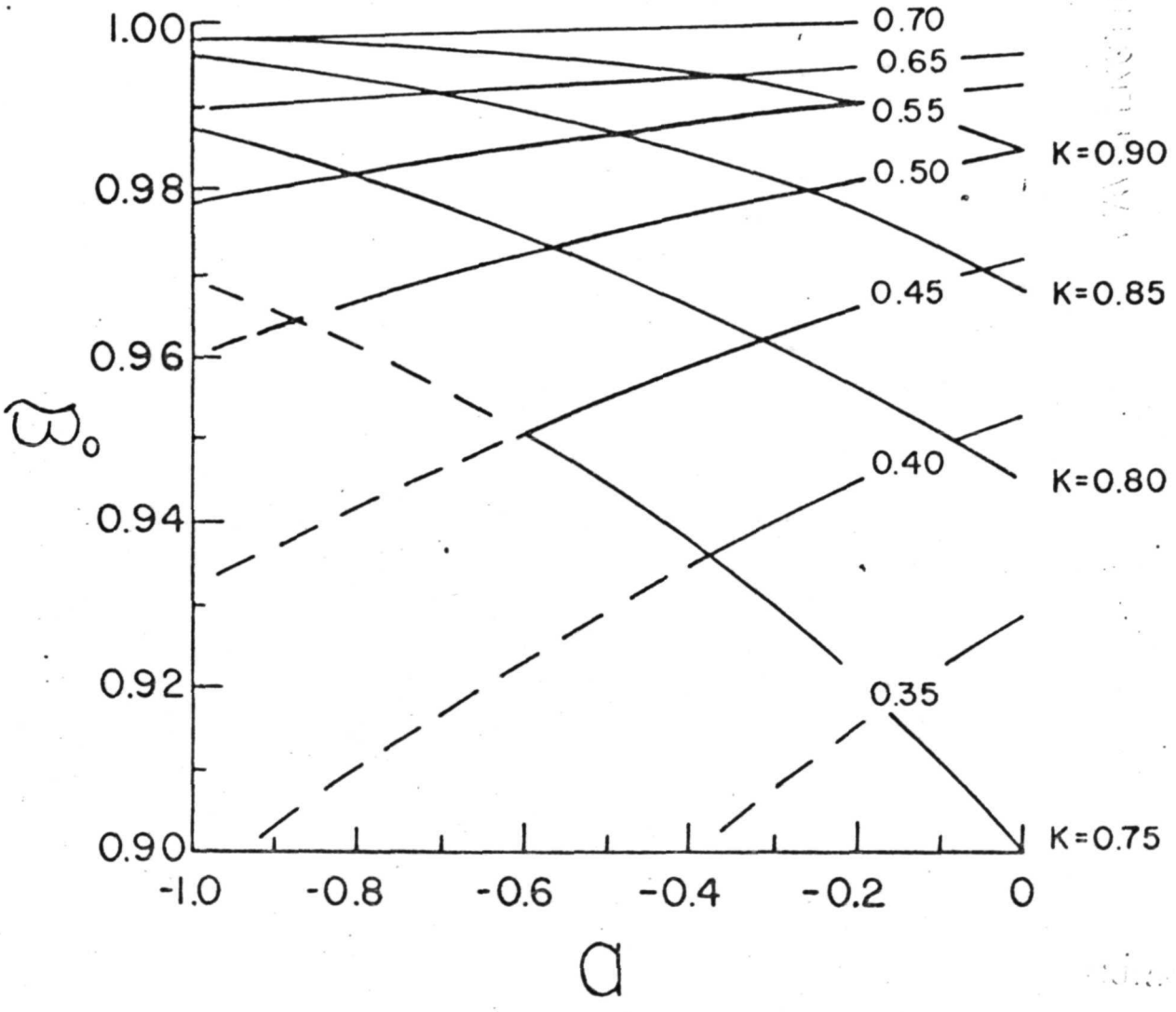
1.00
0.98
0.96
0.94
0.92
0.90
ϖ_o
-1.0
-0.8
-0.6
-0.4
-0.2
0
a
0.70
0.65
0.55
0.50
0.45
0.40
0.35
K=0.90
K=0.85
K=0.80
K=0.75

FIGURE 11

APPENDIX B

THE SCATTERING MEAN FREE PATH IN THE URANIAN ATMOSPHERE

Michael J. Price*
Planetary Science Institute
Tucson, Arizona 85704

* Visiting Astronomer, Kitt Peak National Observatory, which is operated by the Association of Universities for Research in Astronomy, Inc., under contract with the National Science Foundation

Page Intentionally Left Blank

ABSTRACT

New measurements of the equivalent widths of the 4-0 S(0) and S(1) H_2 quadrupole lines in the Uranian spectrum have been obtained using high-dispersion (4.12Å/mm) image-tube spectrography. The measured equivalent widths are 62 ± 6 mÅ and 58 ± 4 mÅ for the S(0) and S(1) lines, respectively. Curve-of-growth analysis in terms of a reflecting layer model yields an H_2 column density of 780 ± 200 km. amagat and a temperature of 78^{+15}_{-10} °K. Interpretation using a semi-infinite, homogeneous, isotropically scattering model for line formation yields a scattering mean free path at λ 6400Å of 550 ± 150 km. amagat. The values derived for the H_2 column density and scattering mean free path are insensitive to atmospheric temperature. In a clear, conservatively Rayleigh scattering, pure H_2 atmosphere, the corresponding scattering mean free path is 692 km. amagat. The results are consistent with the hypothesis that the regions of the Uranian atmosphere probed by visual radiation are essentially devoid of aerosol particles.

I. INTRODUCTION

Some time ago Belton, McElroy and Price (1971) proposed that the region of the Uranian atmosphere probed by visible light is entirely devoid of clouds. Their proposition was based on an analysis of measurements by Giver and Spinrad (1966) of the 4-0 S(0) and S(1) H_2 quadrupole lines. Interpretation in terms of both reflecting layer and simple scattering models for line formation indicated that the atmosphere can be represented by an essentially semi-infinite, clear, pure H_2 model. Using a curve-of-growth analysis for the reflecting layer model, which included the effects of saturation, Belton et al derived an H_2 column-density of 480 km. amagat and an atmospheric temperature of $118 \pm 40^{o}K$. In a detailed discussion of Raman scattering and pressure-induced dipole H_2 opacity sources, Belton et al showed qualitatively that a semi-infinite, pure H_2 model atmosphere is compatible with the general visible and near infrared spectral character of Uranus. To provide for the detailed band structure an additional contribution to atmospheric opacity by gaseous methane is required. Wallace (1972) has pointed out, however, that there are enough uncertainties in both the observational data and theoretical analyses to permit alternative views.

Qualitative support for the clear atmosphere hypothesis comes from direct, high angular resolution ($\pm$ 0.2 arc sec.) imagery of the planet obtained by Danielson, Tomasko and Savage (1972) using a balloon-borne telescope. Except for the presence of strong, symmetrical, limb-darkening, the visual (λ 3800Å - λ 5800Å) appearance of Uranus is of a featureless disk. Although small quantitative discrepancies exist, the magnitude of the limb-darkening is consistent with predictions for a semi-infinite, homogeneous, non-conservative, Rayleigh scattering atmosphere. The planetary radius (25,900 kms) measured by Danielson et al is in good agreement with the optimum value (25,300 kms) derived by Belton et al from the ultraviolet geometrical albedo of Uranus on the basis of a semi-infinite, pure H_2, Rayleigh/Raman scattering model atmosphere. Quantitative support is provided by new measurements by Lutz (1973) of the strengths of the 3-0 S(0) and S(1) H_2 quadrupole lines. Using curve-of-growth analysis for a reflecting-layer model, Lutz obtained several total line-of-sight

column-densities η N(J), where η is the geometrical "air-mass" factor and N(J) is the number of molecules with rotational quantum number J. Specifically, Lutz derived η N(J=0) = 333$\pm$ 190 km. amagat and η N(J= 1) = 640$\pm$ 220 km. amagat. The corresponding atmospheric temperature was T = 111$\pm$30 ^{o}K.

Nonetheless Prinn and Lewis (1973) have argued on thermodynamic grounds that a significant methane haze should be present high in the Uranian atmosphere, with a deep-dense ammonia cloud layer far below. They have also shown that the spectral character of the visible and near IR continuum could be explained in a straightforward way by a cloudy component in the atmosphere. On the basis of measurements of the infrared spectral albedo of Uranus, Binder and McCarthy (1972) suggested that a thin layer of CH_4 crystals might indeed exist high in a predominantly clear atmosphere. Westphal (1972) has cited photoelectric-scanner evidence of limb-brightening in the strong methane band at 0.89 microns to support the hypothesis of an optically thin, high albedo, cloud layer in the Uranian atmosphere. Photographic confirmation of limb-brightening has been obtained by Sinton (1972).

Limb-brightening is, however, predicted for the clear H_2-CH_4 atmospheric model; it occurs in certain wavelength regions by virture of the vertical inhomogeneity which results from pressure-induced opacity sources. Belton and Price (1973) have investigated in detail the variation with wavelength of the center-to-limb intensity profile for the case of a semi-infinite, non-conservative, inhomogeneous, Rayleigh scattering, H_2 - CH_4 atmosphere. Measurement of the wavelengths at which the variation of intensity across the disk changes from limb-darkening to limb-brightening, and vice versa, provides a crucial test of the hypothesis that clouds are absent from the visible atmosphere of Uranus. All of the strong CH_4 bands beyond 7600Å should be limb-brightened, as should the central regions of the CH_4 bands at 6190Å, 6670Å and 7300Å. The observations by Danielson et al, by Sinton, and by Westphal are not, however, sufficiently accurate and numerous, nor made in the critical spectral regions to be conclusive.

To further explore the question regarding the clarity of the Uranian atmosphere, the spectroscopic basis of the cloudless concept is re-examined in this paper. The 4-0 H_2 quadrupole band was selected for further study since the S(0) and S(1) lines lie in a spectral window between the λ6190Å and λ6670Å CH_4 bands which is relatively uncrowded by Fraunhofer, or Telluric, line absorption. The 3-0 H_2 quadrupole band is less suitable since it is difficult to locate the continuum level in that spectral region ($\lambda \sim 8200$Å). New measurements of the equivalent widths of the 4-0 S(0) and S(1) H_2 quadrupole lines are reported. In this analysis, the scattering mean free path is indirectly determined.

II. OBSERVATIONAL DATA

Only Giver and Spinrad (1966) have published measurements of the strengths of the 4-0 S(0) and S(1) H_2 quadrupole lines in the Uranian spectrum. Using the Lick Observatory 120-inch aperture reflector/coude spectrograph system, they obtained two broadened spectra in the vicinity of λ6400Å at a reciprocal dispersion of 8Å/mm. No information was given concerning spectrum width or spectral resolution. Individual uncertainties of ±30 percent quoted for the derived strengths of both lines testify to the difficulty of the observations. Their measurements of the equivalent widths of both lines, as weighted by Belton et al (1971), are listed in Table I.

Much of the problem in obtaining accurate equivalent widths for the H_2 quadrupole lines results from their extreme narrowness. To improve the quality of the observational data, it was decided to obtain new broadened spectra at considerably higher dispersion using the maximum possible spectral resolution. Since high spectral resolution requires a narrow spectrograph slit, long exposure times are required. To maximize spectral resolution within a reasonable exposure time, it was decided to record the spectra using an image tube.

During the night of 1972 May 22/23, an excellent quality high-resolution spectrogram of Uranus in the λ6400Å region was obtained with the Kitt Peak 84-inch aperture reflector/coudé spectrograph system. The spectrum was recorded using an ITT Type F4089 Image Tube located at the focus of the No. 6 camera. Focussed with a permanent magnet assembly, this intensifier has a 40 mm diameter photocathode on a plane parallel, ultraviolet transparent face-plate together with a phosphor output which is coupled by fiber optics to a 2 inch x 2 inch Kodak IIa-D plate. The maximum in the spectral intensity distribution of the phosphor output lies in the region of λ 5200Å. During intensification, the original image on the photocathode does not suffer demagnification. Spatial resolution on the plate corresponds to 40 line pairs/mm (12.5 μm). Using the

first order spectrum, a reciprocal dispersion of 4.12Å/mm on the plate was achieved. During the course of the observations, the angular diameter of Uranus given by the 1972 American Ephemeris and Nautical Almanac was 3".88 arc. During the exposure, the "seeing", defined as the half-intensity diameter of a stellar image, varied in the range 1"-2" arc. A slit width setting corresponding to an angular width of 0".24 arc was chosen; the width projected on the plate was 38 μm. Spectral resolution on the plate was conservatively estimated to be 51 μm(0.21Å) the sum of the spatial resolution of the image tube and the projected slit width. Broadening of the spectrum was carried out, using the No. 8 Decker, over an angular range of 4".6 arc; the corresponding width on the plate was 0.79 mm. A neon light source was used to provide a comparison spectrum. The spectrogram of Uranus was exposed for 150 minutes.

Calibration of the photocathode/phosphor of the image tube was carried out using the moon as a light source. To adequately record the lunar spectrum, an exposure of 30 seconds was required. Plate calibration was carried out with a standard spot sensitometer(13-step). By using a combination of intermediate-band color and neutral density filters, the spectral intensity distribution of the spot sensitometer was matched as far as possible to the Uranian λ6400Å continuum produced by the phosphor of the image tube. Maxima in the respective spectral intensity distributions coincided within $\pm$100Å. Exposure times were matched within a factor 3. Cut from the same original, the Uranian and lunar spectrograms were developed together with the spot calibration plate in D-76 for 15 minutes at 68°F. In view of the wide disparity in exposure times for the Uranian and lunar spectrograms (30 secs-2 1/2 hours), prior experiments were carried out to determine whether the shapes and equivalent widths derived for the absorption lines might be affected by reciprocity failure in the phosphor / photographic plate combination. The experiments were based on recording the Uranian and lunar spectrum near λ4000Å. Using the Utrecht Photometric Atlas of the Solar Spectrum as a standard, no evidence of reciprocity failure was found throughout the relevant range in exposure times.

Density tracings were obtained using a Joyce-Loebl Automatic Recording Microdensitometer Mk.IIIC. For efficient handling of the data, the spectrograms of both Uranus and the moon were digitized. Digital spacing was chosen to provide 2-3 data points per spectral resolution element. Following density-intensity conversion, Uranus/moon ratio spectra were obtained in the immediate vicinities of each of the H_2 quadrupole lines. Each spectrum was normalized to the continuum level associated with the center of the respective H_2 line. In each case, the normalization factor was determined using 30 adjacent continuum data points spread symmetrically on either side of the line. The runs error of their mean was taken as the uncertainty in the location of the continuum at the line center. As such, it may be used as a direct estimate of the uncertainty in the derived equivalent widths. Bear in mind, however, that only one plate was used in the determination of the equivalent widths. The observational data are presented in Figure 1. Equivalent widths for both H_2 lines were determined using the trapezoidal rule, anchored at the digital data points. The results are listed in Table I.

III. ANALYSIS

Treatment of the problem of line formation in planetary atmosphere normally employs either of two distinct atmospheric models - the reflecting layer model or the scattering model. In the reflecting layer model, the atmosphere is assumed to consist of a clear layer of gas overlying a sharply defined, optically thick, cloud layer. The principal attraction of the model is that it utilizes a minimum number of parameters. Besides known line-strength data and geometrical factors, only the column-density of gas, the effective pressure, and the temperature are involved. Iterative application of curve-of-growth theory in the multi-line formation problem will permit the mean atmospheric temperature, effective pressure, and column-abundance of H_2 to be derived. In the scattering model, the atmosphere is assumed to consist of a semi-infinite homogeneous, isotropically scattering, aerosol haze. Compared to the reflecting layer model, an additional parameter - the single scattering albedo in the continuum - must be defined; it is normally obtained by interpreting narrow-band photometric, or spectrophotometric, continuum measurements in terms of a semi-infinite, homogeneous, isotropically scattering atmosphere. Also, the column-density of gas is replaced by the concept of the amount of gas in a scattering mean free path. Information concerning the mean volume density of aerosol particles above the effective level of photon penetration can be obtained. Both models will be used in the analysis. The H_2 column-density obtained from the reflecting layer model will determine whether the effective depth of photon penetration is significantly reduced by cloud particle extinction. The scattering model will provide an estimate of the average scattering mean free path in the regions of the atmosphere probed by visual radiation.

Interpretation of the observational data is based on the curve-of-growth theory for homogeneous atmospheres, each model for line formation being individually considered. For both reflecting-layer and scattering cases,

single values of effective temperature and pressure are used to represent the Uranian atmosphere. The H_2 quadrupole lines' absorption profiles are determined not only by both Doppler-and pressure-broadening but also by the phenomena of collision-narrowing. Following Fink and Belton (1969) and Belton, McElroy and Price (1971), the Galatry (1961) profile will be used to describe the absorption profile. Revised values for the pressure-broadening coefficient at STP, α_0, and the collision-narrowing parameter, z, were adopted from recent work by Belton (1973) on the 1-0 S(1) H_2 quadrupole line. Computations by James (1969) indicate that the corresponding pressure-broadening parameter, α_0, is 1.5×10^{-3} cm^{-1} $amagat^{-1}$. The value of α_0 is taken to vary with pressure, p, and temperature, T, as $pT^{-0.75}$. In the notation of Fink and Belton (1969), z is equal to $2\pi\alpha_L/\beta$, where α_L is the pressure-broadened Lorentz half-width (1/2 full line width), and β is the coefficient of dynamical friction. By definition β is equal to kT/mD, where k is the Boltzmann constant, m is the H_2 molecular mass, and D is the diffusion coefficient. On the basis of new information on the H_2 diffusion coefficient obtained from Murray and Javan (1972), Belton derived a z value of 0.032. Using the revised values of α_0 and z to compute a theoretical curve-of-growth, he satisfactorily fitted the laboratory data on the 1-0 S(1) line obtained by Rank, Fink and Wiggins (1966). Because of the lack of analogous information for the 4-0 S(0) and S(1) lines, the H_2 parameters derived for the 1-0 S(1) line will be used in this analysis.

In the notation of Fink and Belton (1969), the relation between the H_2 quadrupole line equivalent width, W, and the parameters of the radiative transfer model can be written

$$\frac{W}{\alpha_D \sqrt{\pi}} = F\,(u; \mu, \mu_0, y, z, \tilde{\omega}_c) \qquad (1)$$

where α_D is the Doppler width, and u is proportional to the characteristic optical length in the medium at the line center. In the isothermal reflecting layer model, the characteristic length is the scale height; in the scattering model it is the interaction mean free path. Specifically, u is equal to $N\,S(J,T)/\alpha_D \sqrt{\pi}$, where

S(J, T) is the line "strength" containing the Boltzmann population factor for the lower level J of the transition at temperature T. In the reflecting layer model, the characteristic amount of gas, N, is the column-abundance; in the scattering model, it is the photon mean free path. The parameters μ, μ_0 are the cosines of the angles of emergence and immergence, respectively; y is equal to α_L/α_D; and $\tilde{\omega}_c$ is the single scattering albedo, not required in the reflecting layer model.

Interpretation of the observational data in terms of the reflecting layer model closely followed the iterative curve-of-growth technique used by Fink and Belton (1969) to analyze H_2 quadrupole line data for Jupiter. Particular use was made of their "effective-pressure" concept. For the initial application of the curve-of-growth, an atmospheric temperature of 76°K was obtained on the assumption that the S (0) and S (1) lines were unsaturated; an effective pressure of 2 atm. was derived on the assumption that the reflecting layer was located at an H_2 Rayleigh scattering optical depth τ (λ6400Å) = 2. The relevant cross-section was derived from Victor, Browne and Dalgarno(1967). Unit optical depth is equivalent to an H_2 column-density of 692 km amagat. Since the phase angle of Uranus was small, the values of μ, μ_0 were taken equal at unity. Computations of S(J, T) were based on H_2 quadrupole absorption line data given by Dalgarno, Allison, and Browne (1969). With the atmospheric temperature held constant, iterative application of the curve-of-growth to the 4-0 S(1) line lead rapidly to an optimum effective pressure of 3.9 atm., corresponding to a y value of 0.362. Iteration was based on the 4-0 S(1) line since the corresponding $S(J, T)/\alpha_D \sqrt{\pi}$ factor is insensitive at the $\pm$ 5 percent level to temperature variations throughout the range $75^{\circ}K \leq T \leq 150^{\circ}K$; by comparison, the corresponding variation for the 4-0 S(1) line is $\pm$ 50 percent. The final curve-of-growth, together with the observational data, is shown in Fig. 2. Taking into account saturation effects in both the S (0) and S (1) lines, the atmospheric temperature finally adopted was $78\ ^{+15}_{-10}\ ^{\circ}K$. The H_2 line-of-sight abundance derived from the 4-0 S(1) line was then $2791\ ^{+712}_{-547}$ km. amagat. Quoted errors are based on the uncertainties in the measured equivalent widths only.

To derive the H_2 column-density, the line-of-sight abundance must be divided by the air mass factor, η. Because of seeing effects coupled with the small angular diameter of the planet, precise determination of η is not possible. Nevertheless, limitations may be placed on its value by considering two extreme cases. In both, the slit of the spectrograph crosses the diameter of the planet. In the first case, perfect seeing (i.e. no atmospheric angular spreading of near-point light sources) and symmetry with respect to position angle are assumed. The air mass factor is readily shown equal to π. The corresponding H_2 column density is 888^{+227}_{-174} km. amagat. In the other extreme, poor seeing (i.e. light from all regions of the planetary disk is completely "scrambled" before reaching the telescope) is assumed. The η value is 4. The resultant H_2 column-density is 698^{+178}_{-137} km. amagat. In fact, the seeing lies between the two extreme cases so that a mean η value is probably more nearly correct. The H_2 column-density finally adopted is 780 ± 200 km. amagat.

Application of the homogeneous, isotropically scattering model for line formation followed the general procedure used by Fink and Belton (1969) on the basis of theoretical developments by Belton (1968). Determination of the single scattering albedo, $\tilde{\omega}_c$, was based on spectrophotometric measurements of the Uranian geometrical albedo, p, by Younkin (1970) corrected to the planetary radius obtained by Danielson et al (1972). For the case of a semi-infinite, homogeneous, isotropically scattering atmosphere, geometrical albedo is related to the single scattering albedo through the Chandrasekhar (1950) H-functions according to

$$p = \frac{1}{4} \tilde{\omega}_c \int_0^1 \mu_0 \, H^2_{\tilde{\omega}_c}(\mu_0) \, d\mu_0 \qquad (2)$$

The value derived for $\tilde{\omega}_c$ was 0.975. Values selected for y and z were 0.362 and 0.032, respectively. The atmospheric temperature was taken as 78°K. Because of insensitivity of the relevant $S(J,T)/\alpha_D \sqrt{\pi}$ factor to uncertainty in the temperature, determination of the scattering mean free path, N, was based on the measured equivalent width of the 4-0 S(1) line alone.

In analyzing the observational data, the two extremes of "seeing" were considered. For perfect seeing, the theoretical equivalent width, $\overline{W}$, was obtained by averaging across the diameter of the planetary disk according to

$$\overline{W} = \frac{\int_0^{\pi/2} W(\theta)\, I(\theta) \cos\theta \; d\theta}{\int_0^{\pi/2} I(\theta) \cos\theta \; d\theta} \tag{3}$$

where θ ($= \cos^{-1}\mu = \cos^{-1}\mu_0$) is both the angle of emmergence and immergence, $W(\theta)$ is the corresponding equivalent width, and $I(\theta)$ is the corresponding specific continuum intensity. In the case of poor seeing, we have

$$\overline{W} = \frac{\int_0^{\pi/2} W(\theta)\, I(\theta) \sin\theta \cos\theta \; d\theta}{\int_0^{\pi/2} I(\theta) \sin\theta \cos\theta \; d\theta} \tag{4}$$

In each case, the relation between W and N was defined, trial values for the scattering mean free path of 1, 3, 10, 30, 100, 300, 1000, 3000, 10000 km. amagat being used in turn. Six-point Gaussian quadrature was used to perform the numerical integrations. The actual scattering mean free path (λ6400Å) was derived from the observational datum by graphical interpolation. For the case of perfect seeing, the scattering mean free path was 595 $\pm$ 80 km. amagat. For the case of poor seeing, the corresponding value was 560 $\pm$ 80 km. amagat. Quoted errors are based on uncertainty in the measured equivalent width. By carrying out similar computations for the extremes of temperature suggested by the reflecting layer model (i.e. 68°K and 93°K), a better estimate for the uncertainty in the scattering mean free path can be obtained. The value finally adopted was 550 $\pm$ 150 km. amagat. Bearing in mind that in a pure H_2 conservatively Rayleigh scattering atmosphere the scattering mean free path (λ6400Å) is 692 km. amagat, neither model for line formation provides any evidence that aerosol particles inhibit the penetration of visual photons into the Uranian atmosphere. Results from the reflecting layer model suggest that

the deep-dense NH_3 cloud layer predicted by Prinn and Lewis (1973) to occur at H_2 column-densities ~ 370 km. amagat must be much deeper, in fact too deep to be probed. Results from the scattering model support the hypothesis that the regions of the Uranian atmosphere probed by visual radiation are essentially devoid of cloud particles. If the aerosol haze predicted by Prinn and Lewis (1973) to occur at H_2 column-densities less than 119 km. amagat does in fact exist, it is physically and optically too thin to be detected by the H_2 quadrupole lines' technique.

ACKNOWLEDGEMENTS

It is a pleasure to thank M.J.S. Belton for his generosity in making available his comprehensive curve of growth program; L. Goldberg for granting telescope time for the project and for providing access to the facilities of the Computer Laboratory at Kitt Peak National Observatory for the analysis of the observational data; A. A. Hoag for his personal interest in the success of the project; and J. DeVeny and R. Barnes for providing excellent technical support. This research was sponsored by the National Aeronautics and Space Administration under contract NASW-2363.

REFERENCES

Belton, M.J.S. (1968) "Theory of the Curve of Growth and Phase Effects in a Cloudy Atmosphere: Applications to Venus." J. Atmospheric Sciences 25, 596.

Belton, M. J.S. (1973) Private Communication.

Belton, M.J.S. and Price, M.J. (1973) "Limb Brightening on Uranus: A Prediction." Astrophys. J. 179, 965.

Belton, M.J.S., McElroy, M.B., and Price, M.J. (1971) "The Atmosphere of Uranus." Astrophys. J. 164, 191.

Binder, A.B. and McCarthy Jr., D.W. (1972) "The Infrared Spectral Albedo of Uranus." Astrophys. J. 171, L1.

Chandrasekhar, S. (1950) "Radiative Transfer." (Oxford: Oxford University Press.)

Danielson, R.E., Tomasko, M.G., and Savage, B.D. (1972) "High Resolution Imagery of Uranus Obtained by Stratoscope II." Astrophys. J. 178, 887.

Dalgarno, A., Allison, A.C., and Browne, J.C. (1969) "Rotation-Vibration Quadrupole Matrix Elements and Quadrupole Absorption Coefficients of the Ground Electronic States of H_2, HD and D_2." J. Atmospheric Sciences 26, 946.

Fink, U. and Belton, M.J.S. (1969) "Collision-Narrowed Curves of Growth for H_2 Applied to New Photoelectric Observations of Jupiter". J. Atmospheric Sciences 26, 952.

Galatry, L. (1961) "Simultaneous Effect of Doppler and Foreign Gas Broadening on Spectral Lines". Phys. Rev. 122, 1218.

Giver, L. P. and Spinrad, H. (1966) "Molecular Hydrogen Features in the Spectra of Saturn and Uranus." Icarus 5, 586.

James, T.C. (1969) "Calculations of Collision Narrowing of the Quadrupole Lines in Molecular Hydrogen." J. Optical Soc. America 59, 1602.

Lutz, B.L. (1973) "Molecular Hydrogen on Uranus. Observation of the 3-0 Quadrupole Band." Astrophys. J. (In press).

Murray, J.R. and Javan, A. (1972) "Effects of Collisions on Raman Line Profiles of Hydrogen and Deuterium Gas." J. Molecular Spectroscopy 42, 1.

Prinn, R.G. and Lewis, J.S. (1973) "Uranus Atmosphere: Structure and Composition." Astrophys. J. 179, 333.

Rank, D.H., Fink, U., and Wiggins, T.A. (1966) "Measurements on Spectra of Gases of Planetary Interest. II. H_2, CO_2, NH_3 and CH_4." Astrophys. J. 143, 980.

Sinton, W.M. (1972) "Limb and Polar Brightening of Uranus at 8870Å." Astrophys. J. 176, L 135.

Victor, G.A., Browne, J.C., and Dalgarno, A. (1967) "Optical Properties of Molecular Hydrogen." Proc. Phys. Soc. 92, 42.

Wallace, L. (1972) "Rayleigh and Raman Scattering by H_2 in a Planetary Atmosphere." Astrophys. J. 176, 249.

Westphal, J. (1972) Comment at the 3rd Annual Meeting of the AAS - Division of Planetary Sciences, Kona, Hawaii.

Younkin, R.L. (1970) Thesis, University of California at Los Angeles.

TABLE I

H_2 QUADRUPOLE LINES

MEASUREMENTS OF EQUIVALENT WIDTHS

Line	Wavelength (Å)	Equivalent Width (m Å)	
		Price	Giver and Spinrad
(4-0) S(0)	6435.03	62 ± 6	30 ± 8
(4-0) S(1)	6367.80	58 ± 4	41^{+15}_{-9}

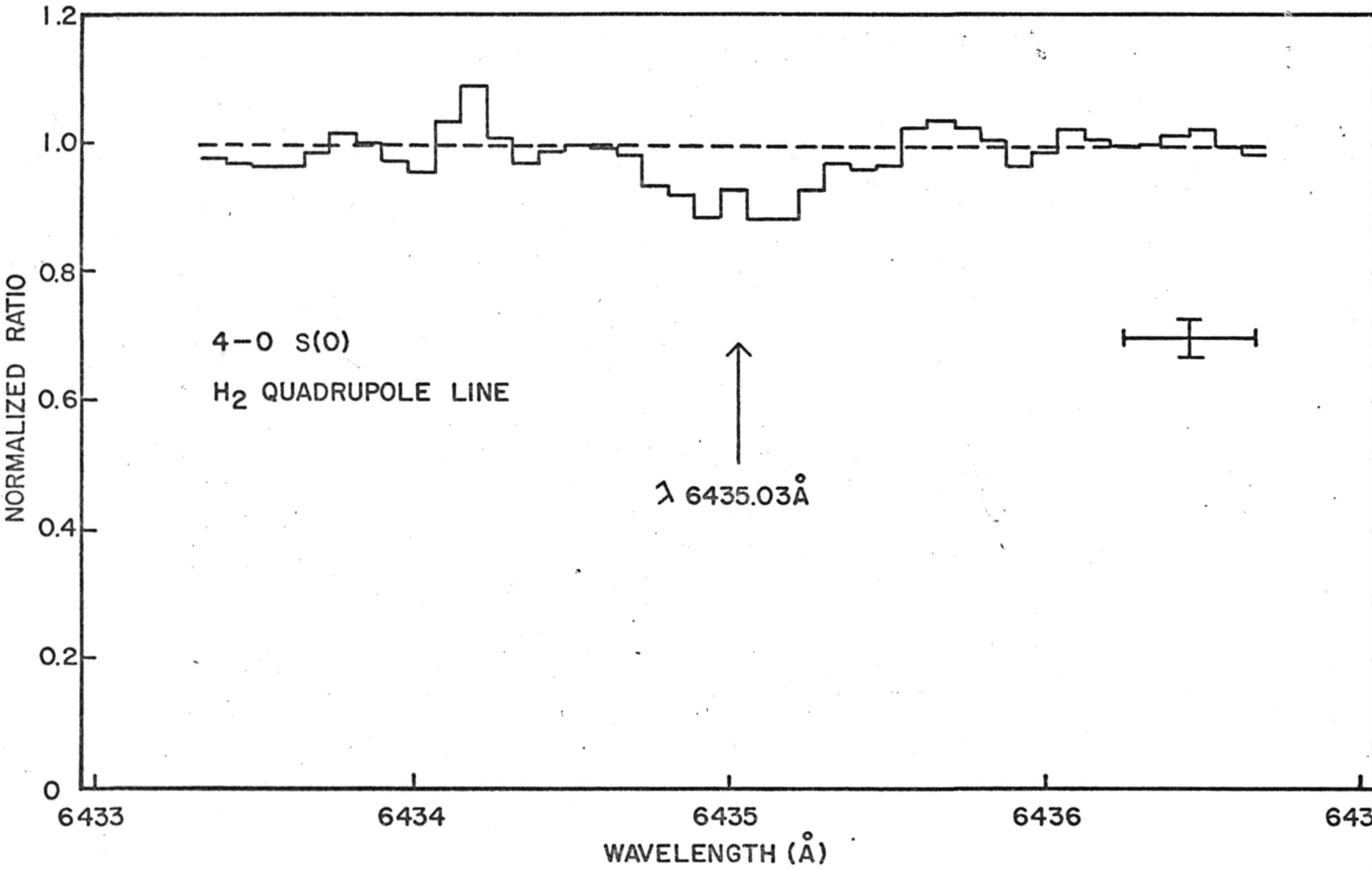
1.2
1.0
0.8
0.6
0.4
0.2
0
NORMALIZED RATIO
4–0 S(0)
H_2 QUADRUPOLE LINE
λ 6435.03Å
6433
6434
6435
6436
643
WAVELENGTH (Å)

Fig I a

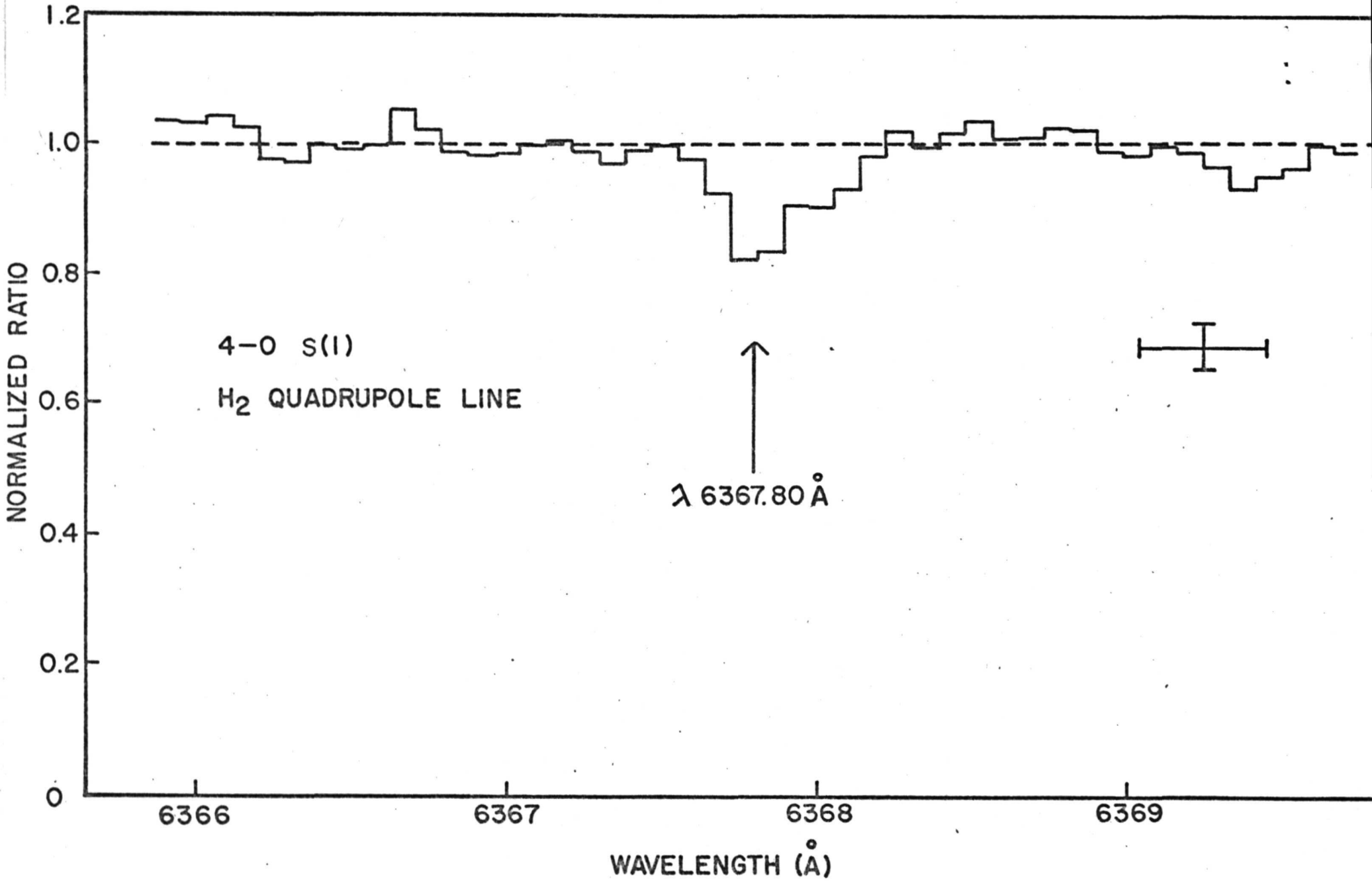
1.2
1.0
0.8
0.6
0.4
0.2
0
NORMALIZED RATIO
4–0 S(1)
H2 QUADRUPOLE LINE
λ 6367.80 Å
6366
6367
6368
6369
WAVELENGTH (Å)

Fig 15

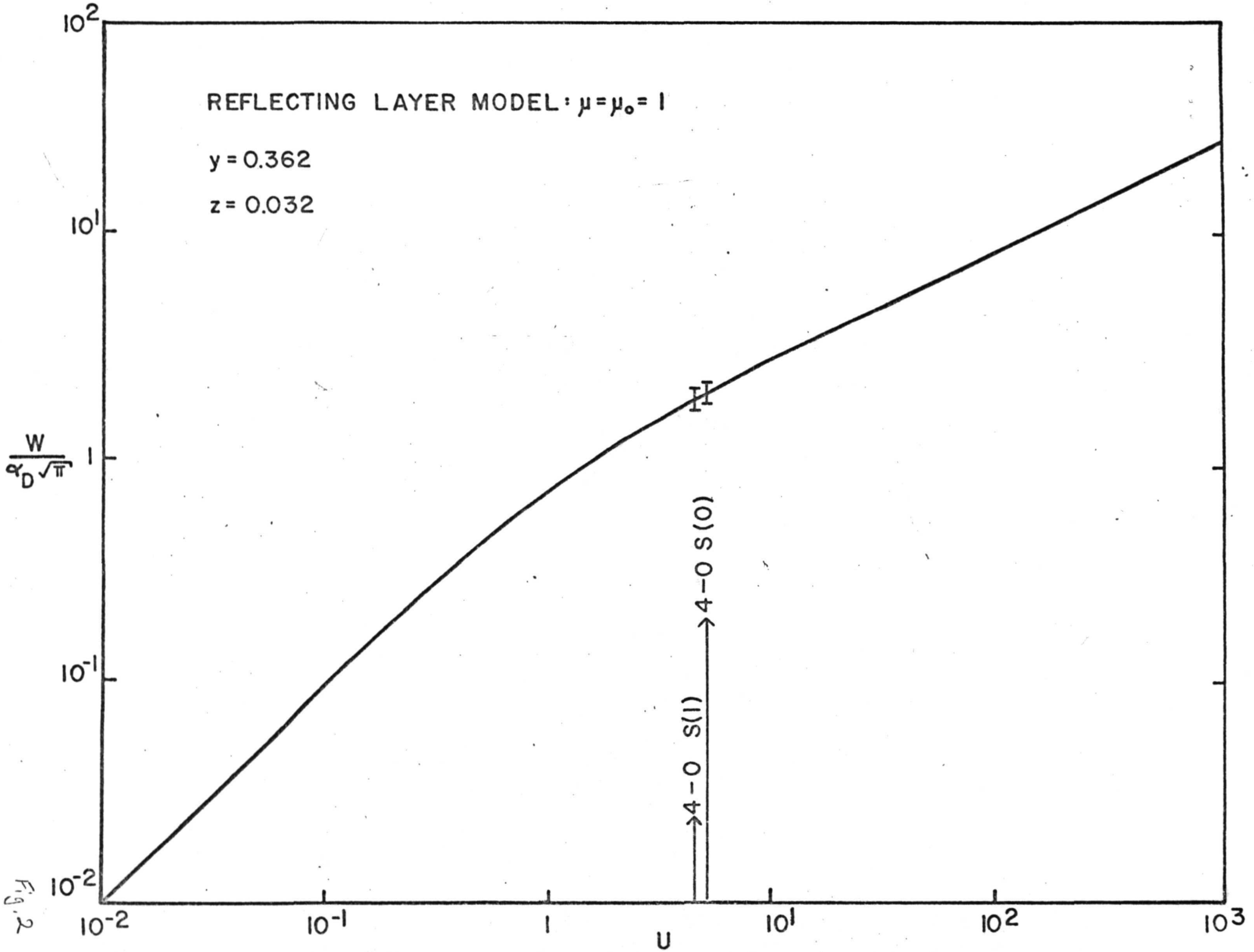
REFLECTING LAYER MODEL: $\mu = \mu_o = 1$
y = 0.362
z = 0.032
$\frac{W}{\alpha_D \sqrt{\pi}}$
10^2
10^1
1
10^{-1}
10^{-2}
10^{-2}
10^{-1}
1
10^1
10^2
10^3
U
4-0 S(1)
4-0 S(0)

Fig. 2

TYPOGRAPHICAL LIST OF SYMBOLS

Paper Title: The Scattering Mean Free Path in the Uranian Atmosphere

Paper Author: M. J. Price

Symbols

$\mathring{A}$	-	angstrom symbol
^{o}K	-	degrees Kelvin
η	-	Greek letter eta
λ	-	Greek letter lambda
$\sim$	-	on the order of
μ	-	Greek letter mu
α_0	-	Greek letter alpha with subscript zero
α_L	-	Greek letter alpha with subscript L
β	-	Greek letter beta
μ_0	-	Greek letter mu with subscript zero
$\tilde{\omega}_c$	-	Special symbol based on Greek letter small omega with superscript $\sim$ and subscript c
α_D	-	Greek letter alpha with subscript D
τ	-	Greek letter tau
θ	-	Greek letter theta